Title

Carotenoid assembly regulates quinone diffusion and the *Roseiflexus castenholzii* reaction center-light harvesting complex architecture

Authors

Jiyu Xin,[1#] Yang Shi,[2#] Xin Zhang,[1,3#] Xinyi Yuan,[1, 3] Yueyong Xin,[3] Huimin He,[3] Jiejie Shen,[1] Robert E. Blankenship,[4] Xiaoling Xu,[1,2]*

Affiliations

[1]Department of Biochemistry and Molecular Biology, School of Basic Medical Sciences and The Affiliated Hospital of Hangzhou Normal University, Hangzhou, 311121, China

[2]Liangzhu Laboratory, MOE Frontier Science Center for Brain Science and Brain-machine Integration, State Key Laboratory of Brain-machine Intelligence & Department of Neurobiology and Department of Pathology of the First Affiliated Hospital, Zhejiang University School of Medicine, Zhejiang University, Hangzhou, 311121, China

[3]Photosynthesis Research Center, College of Life and Environmental Sciences, Hangzhou Normal University, Hangzhou, 311121, China

[4]Departments of Biology and Chemistry, Washington University in St. Louis, St. Louis, MO 63130, USA

[#] These authors contributed equally to this work.

*Correspondence should be addressed to Xiaoling Xu. (xuxl@hznu.edu.cn)

Abstract

Carotenoid (Car) pigments perform central roles in photosynthesis-related light harvesting (LH), photoprotection, and assembly of functional pigment-protein complexes. However, the relationships between Car depletion in the LH, assembly of the prokaryotic reaction center (RC)-LH complex, and quinone exchange are not fully understood. Here, we analyzed native RC-LH (nRC-LH) and Car-depleted RC-LH (dRC-LH) complexes in *Roseiflexus castenholzii*, a chlorosome-less filamentous anoxygenic phototroph that forms the deepest branch of photosynthetic bacteria. Newly identified exterior Cars functioned with the bacteriochlorophyll B800 to block the proposed quinone channel between LHαβ subunits in the nRC-LH, forming a sealed LH ring that was disrupted by transmembrane helices from cytochrome c and subunit X to allow quinone shuttling. dRC-LH lacked subunit X, leading to an exposed LH ring with a larger opening, which together accelerated the quinone exchange rate. We also assigned amino acid sequences of subunit X and two hypothetical proteins Y and Z that functioned in forming the quinone channel and stabilizing the RC-LH interactions. This study reveals the structural basis by which Cars assembly regulates the architecture and quinone exchange of bacterial RC-LH complexes. These findings mark an important step forward in understanding the evolution and diversity of prokaryotic photosynthetic apparatus.

Introduction

Carotenoids (Cars) are natural pigments that play important roles in light harvesting, photoprotection, and assembly of the functional pigment-protein complexes required for photosynthesis. Specifically, Cars capture blue-green light (450-550 nm) and transfer it to chlorophyll or bacteriochlorophyll ((B)Chl) in the light-harvesting (LH) antenna. The excited energy is then transferred to the reaction center (RC) for primary photochemical reactions. In anoxygenic photosynthetic bacteria (PSB), Car-BChl interactions are essential for assembling

the functional LH complexes (Davidson & Cogdell, 1981; Hashimoto, Uragami, & Cogdell, 2016; H. Lang & Hunter, 1994; Walz & Ghosh, 1997). The well-studied purple bacterium *Rhodobacter* (*Rba.*) *sphaeroides* contains a closed LH2 ring comprising nine αβ-polypeptides; each LHαβ noncovalently binds three BChls (two B850s and one B800) and one Car (Qian, Swainsbury, Croll, Castro-Hartmann, et al., 2021). The Car-less strains of *Rba. sphaeroides* are unable to assemble an LH2 complex, indicating that Car-BChl interactions are essential to the maintenance of LH2 structural stability (H. P. Lang, Cogdell, Takaichi, & Hunter, 1995). In the LH1 ring of *Rba. sphaeroides*, a combination of two Car groups forms a tightly sealed, impenetrable fence-like structure that blocks the proposed quinone channel of the closed ring (Olsen, Martin, & Hunter, 2017; Qian, Swainsbury, Croll, Salisbury, et al., 2021). However, there are fewer carotenoids in most LH1 structures, so in *Thermochromatium* (*Tch.*) *tepidum* and *Rhodospirillum* (*Rsp.*) *rubrum* for example, there are small gaps that allow quinones to cross the ring (Niwa et al., 2014; Qian, Croll, et al., 2021; Yu, Suga, Wang-Otomo, & Shen, 2018b). A point mutation in LHα (W24F) dramatically reduces the amounts of LH1-bound Car. However, in the *pufX* knockout strain of *Rba. sphaeroides*, which possesses a closed LH1 ring composed of 17 LHαβs, the same mutation promotes photosynthetic growth (Cao et al., 2022; McGlynn, Hunter, & Jones, 1994; Olsen et al., 2017). These observations indicate a correlation between the number of LH1-bound Cars and the architecture and photochemical functions of the RC-LH1. This phenomenon could be further studied using structural information about Car-depleted RC-LH, but no such data have yet been reported.

Roseiflexus castenholzii is a chlorosome-less filamentous anoxygenic photosynthetic bacterium. It contains only one LH, which forms an unusual RC-LH complex. This complex structurally resembles RC-LH1 but has similar spectroscopic characteristics that are similar to the peripheral LH2 of purple bacteria (Collins et al., 2010; Collins, Xin, & Blankenship, 2009). We previously reported the cryo-electron microscopy (EM) structure of *R. castenholzii* RC-LH at 4.1 Å

resolution. It revealed an RC composed of L, M, and cytochrome (cyt) *c* subunits surrounded by an opened elliptical LH ring of 15 LHαβs, with the tetraheme binding domain of cyt *c* protruding on the periplasmic side. The RC is compositionally larger in purple bacteria than in *R. castenholzii*, in which it does not contain an H subunit (Pugh, McGlynn, Jones, & Hunter, 1998; Qian, Hunter, & Bullough, 2005; Yamada et al., 2005). However, it does contain a unique cyt *c* transmembrane helix (c-TM) and the newly identified subunit X, both of which flank the gap of the LH ring to form a novel quinone shuttling channel (Xin et al., 2018). Notably, the amino acid sequences of subunit X and TM7, a transmembrane (TM) helix separated from the RC-L and RC-M subunits are unassigned. Pigment analyses have revealed a 2:3 Car : BChl molar ratio of *R. castenholzii* RC-LH (Collins et al., 2009). However, the cryo-EM structure resolved only one keto-γ-carotene molecule spanning the interface of each LHαβ, coordinating two B880s and one additional B800 at the periplasmic and the cytoplasmic side, respectively. The lack of a clear cryo-EM density map leaves uncertainty about the presence of additional LH ring-bound Cars, the roles of which are unknown in maintaining the architecture and photochemical functions of the *R. castenholzii* RC-LH.

We here determined cryo-EM structures of native RC-LH (nRC-LH) complexes purified from *R. castenholzii* cells grown under 10,000 lux, 2,000 lux and 100 lux light intensities at 2.8 Å, 3.1 Å and 2.9 Å resolutions, respectively. All three structures shared the same architecture, indicating that the Car composition and assembly are not affected by light intensities. From these high-resolution structures, we identified 14 additional keto-γ-carotene molecules in the exterior of the LH ring ($K\gamma C_{ext}$). In combination with the B800 on the cytoplasmic side, the newly identified $K\gamma C_{ext}$ molecules blocked the proposed quinone channel between LHαβ subunits, forming a sealed LH ring conformation. We also assigned the full amino acid sequences of subunit X, TM7 and an additional TM helix that were derived from hypothetical proteins Y and Z, respectively, and demonstrated their roles in forming the quinone channel and stabilizing the RC-LH

interactions. To investigate the role of Cars in the assembly of RC-LH, *R. castenholzii* cells were treated with Car biosynthesis inhibitor diphenylamine (DPA) to produce a Car-depleted RC-LH (dRC-LH); a 3.1 Å-resolution cryo-EM structure of this complex resolved only five keto-γ-carotene molecules bound in the interior of the LH ring ($K\gamma C_{int}$). The absence of subunit X and $K\gamma C_{ext}$ molecules in the dRC-LH produced a LH ring with exposed LHαβ interface and a larger opening than that of nRC-LH. This conformation accelerated quinone/quinol exchange without affecting the Car-to-BChl energy transfer efficiency. This study thus revealed a previously unrecognized structural basis by which Car assembly regulates the architecture and quinone/quinol exchange rate of the bacterial RC-LH complex. These findings further our understanding of diversity and molecular evolution in the prokaryotic photosynthetic apparatus.

Results

Identification of $K\gamma C_{ext}$ in the nRC-LH complex

To investigate the LH-bound Car numbers and its correlation with the light intensities, we anaerobically cultured *R. castenholzii* cells under the light intensity (2,000 lux) used for obtaining the reported 4.1-Å RC-LH structure (Xin et al., 2018), and also a high and a low light intensity at 10,000 lux and 100 lux, respectively. The cell proliferation rate was much faster under 10,000 lux than that grown under 2,000 lux and 100 lux light intensities, and the cells grown under higher light intensities showed a darker reddish-brown color after 120 h of culturing (Figure 1—figure supplement 1A and B). We then isolated and purified nRC-LH complexes from these cells at the stationary growth phase (Figure 1—figure supplement 1C). Ultraviolet (UV)-visible-near infrared (NIR) spectrophotometry of the isolated nRC-LH complexes showed typical Q_y bands at 800 nm (B800) and 880 nm (B880) and a Q_x band at 594 nm, which corresponded to LH-bound BChls. Notably, Car-associated absorption peaks were detected at 457, 482, and 519 nm (Figure 1—figure supplement 1D). The nRC-LH complexes

purified from cells under 10,000 lux, 2,000 lux and 100 lux showed the same Car absorption spectrum (Figure 1—figure supplement 1E), indicating the pigments content was not affected by light intensities. These nRC-LH complexes were then imaged via cryo-EM, respectively (Figure 1—figure supplements 2 and 3). Using single particle analysis, the nRC-LH structures obtained from the 10,000 lux, 2,000 lux and 100 lux cells were resolved at an overall resolution of 2.8 Å, 3.1 Å and 2.9 Å, respectively (Figure 1—figure supplements 2 to 4, Table 2). Superimposition of the 10,000 lux model with that of 2,000 lux and 100 lux gave root mean square deviation (RMSD) of 1.753 Å and 1.765 Å, respectively, indicating these three structures share the same architecture.

The 15 LHαβ heterodimers formed an opened elliptical ring surrounding the RC, which contained L, M and cyt *c* subunits; the long and short axes were 112 Å and 103 Å, respectively, and a tetraheme binding domain of cyt *c* protruded into the periplasmic space (Figure 1A and B). Similar as in most purple bacteria, the RC contained a photo-reactive special pair of BChls, one accessory BChl, three bacteriopheophytins (BPheos), two MQ-11 (MQ_A and MQ_B) and a newly identified MQc, and an iron atom to mediate the charge separation and subsequent electron transfer (Figure 1C). Each LHαβ non-covalently bound two B880s and one B800 BChl on the periplasmic and cytoplasmic sides (Figures 1C and 2A). In particular, the LH ring bound 15 interior ($K\gamma C_{int}$), 14 exterior ($K\gamma C_{ext}$) Cars, and an additional KγC that inserted between the LHαβ1 and c-TM in all three structures (Figure 1B-D, Figure 1—figure supplement 5, Movie 1), indicating both Car compositions and assembly in the nRC-LH were not affected by light intensities. The low-pass filtered cryo-EM map of nRC-LH minus that of the reported 4.1-Å model showed apparent density differences for the $K\gamma C_{ext}$ (Figure 1—figure supplement 6A and B), indicating the $K\gamma C_{ext}$ molecules were not resolved due to lack of clear EM densities in the 4.1-Å model. Given the similarities between these three nRC-LH structures, we use the 2.8-Å model for following analyses of the nRC-LH structure.

Incorporation of KγC$_{ext}$ and B800s together blocked the LH$\alpha\beta$ interface

Each LH$\alpha\beta$ heterodimer of *R. castenholzii* was stabilized by hydrogen bonding interactions between LHβ-Arg55 and LHα-Asn37 on the periplasmic side, and by LHβ-Gln22 and LHα-Arg4 on the cytoplasmic side (Figure 2—figure supplement 1A). These interactions were not resolved in the 4.1-Å model, due to lack of clear cryo-EM densities for the Arg4 and Arg55 residues. The LH-bound B880s and one B800 BChl were coordinated by highly conserved His residues on the periplasmic and cytoplasmic sides (Figure 2A, Figure 2—figure supplement 1B). Incorporation of an additional B800 at the cytoplasmic side of the LH ring resembles the exterior LHh ring of *Gemmatimonas* (*G.*) *phototrophica* RC-dLH, in which the B800s were oriented perpendicular to the plane of the membrane (Qian et al., 2022). Superposition of each LH$\alpha\beta$ with that of *G. phototrophica* LHh revealed high overlap at the TM helices, with the exception that the B800 porphyrin ring was inclined nearly 60 °relative to the *G. phototrophica* LHh-bound B800 (Figure 2B). Notably, the B800 conformation was also different from that of B800s bound in *Rba. sphaeroides* LH2 and *Rhodopseudomonas (R.) acidophila* LH3, in which the porphyrin rings were both oriented towards the center of the LH ring (Figure 2—figure supplement 1C). Compared to *Tch. tepidum* RC-LH1 that contains a closed LH1 ring, the B800s occupied the space of an N-terminal helix of LH1-α and the head of an ubiquinone (UQ) bound in the LH$\alpha\beta$ interface (Figure 2C). Thus, incorporation of the B800s in nRC-LH occupied the LH$\alpha\beta$ interface on the cytoplasmic side.

Notably, keto-γ-carotenes in the LH ring of nRC-LH were located at two distinct positions (Figures 1D and 2D). 15 keto-γ-carotene (KγC$_{int}$) molecules obliquely spanned the LH$\alpha\beta$ subunits, with the 4-oxo-β-ionone rings sandwiched between adjacent LH$\alpha\beta$s and the ψ-end groups directed into the LH center. In addition, another 14 keto-γ-carotenes were detected in a second position in the LH ring exterior (KγC$_{ext}$), which were almost parallel to the adjacent LHβ subunits; the 4-oxo-β-ionone rings were directed toward the cytoplasmic side and the ψ-end

groups stretched into the periplasm (Figure 2D). Alternatively, a newly identified keto-γ-carotene (KγC) was sandwiched between LHαβ1 and c-TM, with its 4-oxo-β-ionone ring directing towards the RC-Y subunit (Figure 2E). The B-factor was higher for $K\gamma C_{ext}$ than for $K\gamma C_{int}$ molecules, with the latter having lower conformational flexibility (Figure 2—figure supplement 2A). Identification of these Cars yielded in a Car : BChl ratio of approximately 1:1.6 for the nRC-LH structure; this was consistent with results from previous pigment studies (Collins et al., 2009). High performance liquid chromatography (HPLC)-Mass spectrometry (MS) analyses of the pigments in nRC-LH revealed a typical BChl peak at the retention time of 5.58 min, and several peaks of γ-carotene and its derivatives (Figure 2—figure supplement 3). In respect to the complicated Car compositions and lack of specific absorption coefficients of the derivatives, it is impracticable to quantify the Car : Bchl ratio from nRC-LH solution.

The nRC-LH thus resembled *Rba. sphaeroides* RC-LH1, which also binds two groups of Cars with different configurations (Tani, Nagashima, et al., 2021). Superposition analyses revealed similar Car positions and orientations between these two structures, although the keto groups of both Car types in nRC-LH were shifted toward the LHα subunits by ~6.7 Å (Figure 2—figure supplement 4A and C). Although $K\gamma C_{ext}$ molecules were not well aligned with the LHαβ-bound ubiquinone (UQ) molecule in *Tch. tepidum* RC-LH1, they occupied the space between adjacent LHβs (Figure 2C, Figure 2—figure supplement 4B and D). As a result, the $K\gamma C_{ext}$ molecules and additional B800s in *R. castenholzii* nRC-LH together blocked the LHαβ interface (Figure 2F), which serves as the quinone channel for the closed LH1 ring (Qian et al., 2022; Yu et al., 2018b), and for the opened LH1 ring bound only with interior Cars (Qian, Croll, et al., 2021; Swainsbury et al., 2021; Yu et al., 2018b).

Assignment of the subunit X in nRC-LH complex

The *R. castenholzii* nRC-LH is distinguished from the RC-LH1 of most purple photosynthetic bacteria by a newly identified subunit X and a membrane-bound cyt *c*, which has the TM helices

that insert into the gap between LHαβ1 and LHαβ15 to form a putative quinone shuttling channel to the membrane quinone pool (Xin et al., 2018). Unlike the *Rba. sphaeroides* RC-LH1 protein PufX, which interacts with both LH1 and the L and H subunits of the RC (Cao et al., 2022; Tani, Kanno, Kikuchi, et al., 2022), subunit X in *R. castenholzii* was an independent TM helix that did not show any spatial overlap with PufX and PufY from the monomeric *Rba. sphaeroides* RC-LH1 (Figure 2—figure supplement 4E). Furthermore, compared with *Tch. tepidum* RC-LH1, which contains a closed LH1 ring, the c-TM of *R. castenholzii* nRC-LH was positioned close to the 16th LH1-α, whereas subunit X showed no overlap with the 16th LH1-β (Figure 2—figure supplement 4B). These structural features indicated that *R. castenholzii* RC-LH has evolved different quinone shuttling mechanisms. However, the amino acid sequence of subunit X was unassigned in our previous 4.1-Å model, due to lack of clear cryo-EM densities.

From the high-resolution structure of nRC-LH, we successfully assigned the amino acid sequence (Met1-Ser26) for subunit X, which was derived from a hypothetical protein containing 32 amino acid residues (Figure 2G and H). This polypeptide was encoded by coding sequences (CDS: 1,060,366-1,060,464) in *R. castenholzii* (strain DSM 13941/HLO8) genome, but it was not annotated in the Protein Database of Uniprot and NCBI. The amino acid sequence of subunit X showed strict conservation with a hypothetical protein KatS3mg058_1126 (GenBank: GIV99722.1) from *Roseiflexus sp.*, which was denoted by metagenomic analyses of the uncultivated bacteria in Katase hot spring sediment (Kato, Masuda, Shibata, Shirasu, & Ohkuma, 2022) (Figure 2—figure supplement 5). The resolved subunit X inserted into the LH opening in opposite orientation with that of LHαβ and c-TM, where these TM helices were stabilized by hydrophobic and weak hydrogen bonding interactions (Figure 2G and I). On the cytoplasmic side, the C-terminus of subunit X was coordinated in a pocket formed by the cyt *c* N-terminal region (Leu8, Phe9 and Thr13), LHβ15 (Val25 and Ile28), and the 4-oxo-β-ionone ring of a KγC_{int} molecule. A weak hydrogen bond (3.5 Å) formed between the Met25 main chain nitrogen

of subunit X and Arg19 amino nitrogen of c-TM. These pigment-protein interactions together stabilized the conformation of subunit X (Figure 2I, Movie 2).

Stabilizing the RC-LH interactions by newly assigned proteins Y and Z

Superposition of the RC structure with that of purple bacteria showed excellent matches at the L and M subunits, each of which contained five TM helices. Unlike purple bacteria, *R. castenholzii* L and M subunits are encoded by a fused gene *puf LM* but processed into two independent peptides in the complex (Collins et al., 2010; Collins et al., 2009; Yamada et al., 2005). In current model, RC-L subunit contains TM1-5 and terminates at Ala315, whereas the TM6-10 composed RC-M starts from Pro335 (Figure 3A, Figure 3—figure supplement 1A and C). In addition, *R. castenholzii* RC-L contains an N-terminal extension (Met1-Pro35) that was solvent exposed on the cytoplasmic side (Figure 3B, Figure 3—figure supplement 1A and C). Most importantly, we resolved two additional TM helices in the RC (Figure 3A). Near the TM5 from RC-L and c-TM, a separate TM helix (corresponding to the TM7 in previous 4.1-Å model) was resolved with amino acid residues (Met1-Pro32) from a hypothetical protein Y (Figure 3C). Similar as subunit X, this protein was encoded by CDS (1,089,486-1,089,602) from *R. castenholzii* (strain DSM 13941/HLO8) genomic DNA, but it was not annotated in Protein Database as well. Coincidently, the amino acid sequence of protein Y was conserved with a hypothetical protein KatS3mg058_1154 (GenBank: GIV99750.1) from *Roseiflexus sp.* (Figure 2—figure supplement 5). The N-terminal region of protein Y was inclined towards the c-TM on the periplasmic side, wherein the 4-oxo-β-ionone ring of KγC was coordinated by hydrogen bonding interactions with Met11 (3.4 Å) from Y, Ser35 (3.0 Å) and Trp40 (2.8 Å) from the c-TM. On the cytoplasmic side, protein Y was stabilized by hydrogen bonding interactions with the TM5 of RC-L (Figure 3B).

Unlike purple bacteria, *R. castenholzii* RC does not contain an H subunit. Instead, we identified an individual TM helix between the LHα11 and RC-M (Figures 1B and 3D-E). Superposition

revealed mismatch of this TM helix with that of the purple bacterial H subunit (Figure 3A). This helix was assigned to cover the amino acid residues Ser12 to Asn58 of a hypothetical protein (WP_041331144.1) from *R. castenholzii* (strain DSM 13941/HLO8) (Figure 3D), we named it protein Z. This protein was verified with a sequence coverage of 19 % by peptide mass fingerprinting (PMF) analyses of the Blue-Native PAGE of nRC-LH (Table 1). The resolved protein Z was stabilized by hydrogen bonding and hydrophobic interactions with amino acid residues from the RC-M and LHα11 on the periplasmic and cytoplasmic sides (Figure 3E).

In contrast with most purple bacteria, *R. castenholzii* cyt *c* contains an N-terminal transmembrane helix c-TM, which was absent in *G. phototrophica* and *Tch. tepidum* RC-bound cyt *c*, and was even distinct from *Rhodopila* (*Rpi.*) *globiformis* cyt *c* that also contains an N-terminal TM helix (Tani, Kanno, Kurosawa, et al., 2022) (Figure 3F, Figure 3—figure supplement 1B and C). Compared to *Rpi. globiformis* cyt *c*, the c-TM was obliquely inserting into the LH opening in an opposite direction, wherein it formed a potential quinone shuttling channel with the subunit X (Figure 3F). The N-terminal cytoplasmic region of c-TM was stabilized by extensive hydrophobic interactions with LHαβ15 and LHαβ1 (Figure 2I). These included interactions between the cyt *c* Ile27, Phe20, and Val16 sidechains and the LHβ1 Trp14, Leu17 and Pro16 sidechains. The main chain oxygen of Leu8 formed a hydrogen bond with the guanidine nitrogen of Arg9 from LHα15 (3.2 Å). Notably, cyt *c* also formed extensive hydrogen bonding interactions with the RC-L and RC-M subunits at the heme3-binding region (Figure 3—figure supplement 2A). In addition to the protein Y, Z and cyt *c* mediated interactions, another two close contact points were evident between the RC and LH; (i) helix 1 (TM1) from RC-L to LHα13, (ii) TM6 from RC-M to LHα4 and LHα5 (Figure 3—figure supplement 2B). We also identified several structured lipids (phosphatidylglycerol, PG; and diglyceride, DG) within the interface between the RC and LH subunits (Figure 3G and H), these protein-lipids contacts further stabilized the nRC-LH complex.

Car-depleted RC-LH (dRC-LH) lacked subunit X

To explore the structural and functional relationships between LH-bound Cars and the RC-LH complex, *R. castenholzii* cells were photoheterotrophically cultured in the presence of DPA, a Car biosynthesis inhibitor for photosynthetic bacteria (Gall, Henry, Takaichi, Robert, & Cogdell, 2005). In response to DPA-treatment, bacterial growth curves clearly indicated a decreased proliferation rate of cells grown under 10,000 lux, confirming the important roles of Cars in photosynthesis and cell proliferation (Figure 1—figure supplement 1A and B). Interestingly, DPA treatment did not affect the growth of cells illuminated under 2,000 lux and 100 lux, which showed an overall much lower proliferation rate (Figure 1—figure supplement 1B). Concomitantly, the color of the growing cells changed progressively from brownish red in the first culture to light yellow in the fifth sub-culture (Figure 1—figure supplement 1A), indicating gradual inhibition of Car biosynthesis during sub-culturing. To confirm the effects of DPA treatment on Car incorporation into the RC-LH, dRC-LH complexes were isolated from each successive sub-culture of DPA-treated *R. castenholzii* cells (Figure 1—figure supplement 1F). There was a striking decrease in Car absorbance in dRC-LH complexes extracted from the third through fifth sub-cultures of DPA-treated cells compared to nRC-LH extracted from untreated cells (Figure 1—figure supplement 1D and E). Additionally, HPLC analysis of dRC-LH isolated from the fifth sub-culture of DPA-treated cells showed same pigment compositions but decreased absorbance compared to the nRC-LH (Figure 2—figure supplement 3B).

To illustrate the effects of DPA treatment on the RC-LH architecture, we determined the cryo-EM structure of dRC-LH isolated from the fifth sub-culture of DPA-treated *R. castenholzii* cells at 3.1 Å resolution (Figure 4A and B, Figure 4—figure supplement 1). The most obvious difference between these two structures was the absence of the entire X subunit and the cytoplasmic region of cyt *c* subunit (Pro6-Val16) in the dRC-LH; both were located at the LH opening of nRC-LH (Figure 4C, Movie 2). Notably, only five $K\gamma C_{int}$ molecules were resolved

(which spanned the LHαβ5, 7, 9, 10 and 11 heterodimers in the dRC-LH structure), whereas none of the KγC$_{ext}$ molecules were observed (Figure 4B, Figure 1—figure supplement 4C, Movie 1). The five existing KγC$_{int}$ molecules were located relatively far from the LH opening (~52 Å), which is where Cars with the highest B-factors were distributed, indicating an unstable conformation (Figure 2—figure supplement 2A). Additionally, the five KγC$_{int}$ molecules in dRC-LH adopted the same conformation and a similar edge-to-edge distance from LH-bound B800/B880s as the corresponding KγC$_{int}$ molecules did in nRC-LH (Figure 4D, Tables 3 and 4). The absence of KγC$_{ext}$ and most KγC$_{int}$ molecules in the LH ring confirmed that DPA treatment decreased the numbers of LH-bound Cars in the dRC-LH.

The dimensions of the LH ring in dRC-LH increased by ~3.0 Å at the major axes and by ~2.0 Å at the minor axes, although both the protein subunits and cofactors in the RC adopted the same conformations as they did in nRC-LH (Figure 5—figure supplement 1A). Moreover, the distances between adjacent LHαs and LHβs in the dRC-LH showed average increases of 0.5 Å and 1.0 Å, respectively, compared with nRC-LH (Table 5). Accordingly, the Mg-to-Mg distances between adjacent B880s and B800s also increased in dRC-LH (Tables 6 and 7). Specifically, the LH-bound B880s and B800s shifted away from the LH ring center by ~2.0 Å, consequently increasing the Mg-to-Mg distance between LH-bound B880s and the nearest special pair of BChls in the RC (Figure 4E, Table 8). These results therefore indicated that Car depletion not only decreased the number of LH-bound Cars, but also altered the conformation of dRC-LH. These alterations could affect the efficiency of energy transfer during the primary photochemical reactions (Sener et al., 2011; Xin, Pan, Collins, Lin, & Blankenship, 2012).

Conformational changes in the dRC-LH accelerated quinone/quinol exchange

In nRC-LH, insertion of the c-TM and subunit X at the LH opening, wherein the N-terminal cytoplasmic region of c-TM was stabilized by extensive hydrophobic and weak hydrogen bonding interactions with subunit X, LHαβ15 and LHαβ1(Figures 2I and 4C). The c-TM was

closer to LHα1 (9.7 Å) than to LHα15, whereas subunit X was closer to LHβ15 (11.2 Å), creating a narrow gap between the c-TM and the LHαβ15 (Figure 4C and F, Table 5). The B800 pigment was not detected between c-TM and LHα15 (Figure 4C). Thus, the c-TM and subunit X were positioned to the sides of LHα1 and LHβ15, respectively; this formed a 19.4-Å gap between the c-TM and LHα15, and a 28-Å gap between subunit X and LHβ1, both of which may have allowed reduced quinones to exit the LH to the membrane quinone pool. Because dRC-LH lacked subunit X, the gap between LHβ1 and LHβ15 increased to ~38.0 Å (Figure 4C and F). To investigate the functional effects of this conformational change, we compared the quinone/quinol exchange rates for nRC-LH and dRC-LH complexes. In the cyclic electron transport chain of *R. castenholzii*, the periplasmic electron acceptor auracyanin (Ac) transfers electrons back to the RC special pair through the tetra-heme of cyt *c* subunit, reducing the photo-oxidized special pair for turnover of the photo-reaction and electron transfer that subsequently reduce the bound menaquinones (MQ_A and MQ_B) in the RC. The reduced MQH_2 is released from its binding site and exchanges with free MQs outside the RC-LH (Figure 4G). Using sodium dithionite-reduced Ac as the electron donor and menaquinone-4 as the electron acceptor, we measured Ac absorbance changes at 604 nm with varied concentrations of menaquinone-4 (Figure 5—figure supplement 1B and C). The initial oxidation rate of Ac was markedly higher in the presence of dRC-LH than nRC-LH (Figure 4H). This was consistent with the determined apparent Michaelis constants, which showed that dRC-LH had an accelerated quinone/quinol exchange rate of 6.12 ±0.62 μM min^{-1} (Table 9). The accelerated quinone/quinol exchange rate in dRC-LH was probably resulted from exposure of the LHαβ interface by Cars depletion, and also the increased gap dimension of the LH ring.

Carotenoid depletion did not affect the Car-to-BChl energy transfer efficiency

To elucidate the effects of Cars depletion on the Car-to-BChl energy transfer efficiency of the RC-LH, we firstly examined the configurations and coordinating environments of the LH-bound

Cars. KγC$_{int}$ molecules spanned the TM region of each LH$\alpha\beta$ heterodimer; the heads were inserted into the hydrophobic pocket formed by the LHα and LHβ subunits, the phytol tails of two B880s, and the B800 porphyrin ring. On the periplasmic side, the ψ-end group of KγC$_{int}$ was directed into a hydrophobic patch formed by two adjacent LHα subunits (Figure 5A left). Alternatively, the newly-identified KγC$_{ext}$ molecules were immobilized in a position that was nearly parallel to the adjacent LHβs. The heads were inserted into a cavity formed by the B800 porphyrin ring and two adjacent LHβs, and their tails extended along the adjacent LHβs, stabilized by hydrophobic interactions (Figure 5A right). However, depletion of these KγC$_{ext}$ molecules in dRC-LH prevented the tight packing of the KγC$_{int}$ molecules with LH$\alpha\beta$ heterodimers. Thus, in the absence of KγC$_{ext}$, the head of each KγC$_{int}$ molecule shifted towards the B800 porphyrin ring, which moved the head out from the center of the LH ring by ~3.0 Å (Figure 5B). However, the edge-to-edge distances of KγC$_{int}$ to the B800/B880s remained similar between dRC-LH and nRC-LH (Table 3).

We next measured the fluorescence excitation and absorption spectra of the nRC-LH and dRC-LH complexes to calculate the Car-to-BChl energy transfer efficiency. Most RC-LH fluorescence is emitted from the B880 Qy band (Collins et al., 2009). Excitation of nRC-LH at 470 nm yielded emissions at 900 nm, whereas dRC-LH excitation produced emissions at 905 nm (Figure 5C). This shift of the emission peak indicated changes in the LH ring pigment configuration between the two complexes. The intensity ratio of fluorescence excitation spectra to absorption spectra, expressed as the 1-T of RC-LH, was then calculated. The results revealed that the Car-to-BChl energy transfer efficiency remained similar between nRC-LH (44%) and dRC-LH (46%) (Figure 5D). Car-to-BChl energy transfer in the LH is closely related to the number of Car conjugated double bonds, the relative distances between Cars and BChls, and Car/BChl spatial organization (Polivka & Frank, 2010). In *R. castenholzii*, each keto-γ-carotene contains 11 conjugated double bonds (Collins et al., 2009). Although all KγC$_{ext}$ and most KγC$_{int}$

molecules were depleted in dRC-LH, the five remaining KγC$_{int}$ molecules adopted the same configuration and similar edge-to-edge distances with LH-bound B800/B880s as that in the nRC-LH (Figure 4D, Table 3). Therefore, Car depletion from the LH ring in dRC-LH did not affect interactions between the remaining Cars and BChls, which exhibited similar excitation energy transfer values in dRC-LH and nRC-LH complexes. These results suggested that the existing Car-to-BChl energy transfer efficiency is similar even though there is variation in the number of LH-bound Cars.

Discussion

Unlike the well-studied purple photosynthetic bacteria, which contain two types of LH complexes, *R. castenholzii* contains only one RC-LH complex for light harvesting and primary photochemical reactions. It does not contain the H subunit that is typically found in purple bacteria (Pugh et al., 1998; Qian et al., 2005; Yamada et al., 2005). Especially, *R. castenholzii* RC-LH contains a tetra-heme cyt *c* subunit that interrupts the LH ring, which is composed of 15 $\alpha\beta$-polypeptides, through a novel N-terminal TM helix; together with the newly identified subunit X, this forms a potential quinone shuttling channel on the LH ring. In the present study, we determined high resolution cryo-EM structures of nRC-LH, from which we assigned the full amino acid sequence of subunit X, and two additional TM helices derived from hypothetical proteins Y and Z in the RC, which both functioned in stabilizing the RC-LH interactions. Most importantly, we identified 14 additional keto-γ-carotene molecules (KγC$_{ext}$) in the LH ring exterior, and one KγC inserted between LH$\alpha\beta$1 and c-TM, which generated a 2:3 Car : BChl molar ratio consistent with previous pigments analyses (Collins et al., 2009). Binding of the internal and external keto-γ-carotenes together with the B800s blocked the proposed quinone channel between LH$\alpha\beta$ subunits. DPA treatment of the cells yielded a Car-depleted RC-LH, referred to as dRC-LH; a 3.1-Å resolution cryo-EM structure resolved only five KγC$_{int}$

molecules, and the absence of subunit X and the cytoplasmic region of c-TM. These alterations in the dRC-LH increased the size of the LH opening and exposed the LHαβ interface, accelerating the quinone/quinol exchange rate, without affecting the Car-to-BChl energy transfer efficiency.

To maintain continuous photo-reaction and turnover of the electron transport chain, two quinone exchange/transport routes are required for the bacterial RC-LH1 complex. One is the exchange route for the free/bound quinone in the RC, which was represented by a newly identified MQc in our nRC-LH structure (Figure 3H), and also extra ubiquinone molecules found in many purple bacterial RCs (Cao et al., 2022; Kishi et al., 2021; Qian et al., 2022; Qian, Siebert, Wang, Canniffe, & Hunter, 2018; Swainsbury et al., 2021; Tani, Kanno, Kurosawa, et al., 2022; Yu, Suga, Wang-Otomo, & Shen, 2018a). The other one is shuttling channel between the inside and outside of the LH1 ring. For *Tch. tepidum* RC-LH1 that contains an almost symmetric and completely closed LH1 ring, except the 'waiting' UQ8 identified near Q_B, one UQ8 was found to be inserted between the LH1α and LH1β subunits (Yu et al., 2018a), representing a potential quinone exchange channel between the LHαβ interface. Therefore, the space between the LHαβ subunits can serve as quinone exchange channel for the closed LH1 ring (Qian et al., 2022; Yu et al., 2018b), and also for the opened LH1 ring bound only with interior Cars (Qian, Croll, et al., 2021; Swainsbury et al., 2021; Yu et al., 2018b). For most purple bacterial RC-LH1 complexes with an opened C-shaped LH1 ring, reduced quinones are also shuttled from the RC through a gap at the LH1 ring, which is disrupted by protein W, or PufX and PufY (or protein -U) (Cao et al., 2022; Jackson et al., 2018; Qian, Croll, et al., 2021; Tani, Kanno, et al., 2021; Tani, Kanno, Kikuchi, et al., 2022; Tani, Nagashima, et al., 2021).

Distinct from the RC-LH1 of most purple bacteria, each LHαβ of *R. castenholzii* non-covalently bound an additional B800 BChl at the cytoplasmic side, which occupied the LHαβ interface at the cytoplasmic side (Figure 2C, Figure 2—figure supplement 1C). In addition, we identified

426 keto-γ-carotenes at three distinct positions in the nRC-LH ring: internal ($K\gamma C_{int}$) and external
427 ($K\gamma C_{ext}$), and also an additional KγC near the LH opening (Figures 1D and 3B). The $K\gamma C_{int}$
428 molecules embedded between the LHαβs had a similar conformation as they do in the
429 completely closed and also the opened LH1 ring of purple bacteria. In contrast, $K\gamma C_{ext}$ molecules
430 occupied the space between adjacent LHβs, although they were not well aligned with the *Tch.*
431 *tepidum* LHαβ bound UQ8 molecule (Figure 2C, Figure 2—figure supplement 4D). Therefore,
432 incorporation of the $K\gamma C_{ext}$ molecules and additional B800s in *R. castenholzii* nRC-LH together
433 blocked the LHαβ interface for quinone exchange (Figure 2F). Alternatively, *R. castenholzii* RC-
434 LH incorporated a membrane-bound cyt *c* and a hypothetical protein X, which has the TM
435 helices that interrupted the LH ring to form a narrow channel for controlled quinone/quinol
436 exchange (Figure 6). Superposition of *R. castenholzii* with purple bacterial RC-LH1s revealed
437 distinct locations and orientations of subunit X and c-TM compared to PufX and PufY (Figure
438 2—figure supplement 4E), indicating *R. castenholzii* has evolved different quinone shuttling
439 mechanisms.
440 Genetic depletion of the LH1-bound Cars promoted the photosynthetic growth of a PufX-
441 knockout *Rba. sphaeroides* mutant with a closed LH1 ring (Cao et al., 2022; McGlynn et al.,
442 1994; Olsen et al., 2017); this implies that disruption of Cars binding exposed the blocked
443 quinone channel between LHαβ interface and facilitated the quinone exchange, thus promoting
444 photosynthetic growth. In our study, depletion of the $K\gamma C_{ext}$ and most $K\gamma C_{int}$ molecules by DPA
445 treatment could also expose the space between LHαβ subunits. In addition, absence of the
446 subunit X and cytoplasmic region of c-TM in dRC-LH broadened the dimensions of the LH ring
447 opening, which together accelerated the quinone/quinol exchange rate of the dRC-LH (Figure 6).
448 This was consistent with a previous observation that the open form of the *Rhodopseudomonas*
449 (*Rps.*) *palustris* RC-LH1 has a faster quinone diffusion rate than the closed form (Swainsbury et
450 al., 2021). Notably, depletion of most LH-bound Cars only affected the stable conformation of

the cytoplasmic region of c-TM, which was closely associated with subunit X to form the quinone channel (Figure 2I). Compared to cyt *c* subunit that formed extensive hydrogen bonding interactions with the L, M and Y of the RC, the subunit X was characterized by high B-factors, fewer contacts with the RC-LH, and an easily disrupted conformation (Figures 3B and 4C, Figure 2—figure supplement 2B). Especially, the subunit X was derived from a hypothetical protein that inserted into the LH opening in an opposite orientation with LHαβ and c-TM, suggesting that it was likely the last subunit incorporated into the RC-LH. Therefore, *R. castenholzii* RC-LH could evolve the subunit X to control the conformation of the quinone shuttling channel.

Cars contribute to the self-assemble of natural α/β polypeptides to form LH1 complexes in vitro (Fiedor, Akahane, & Koyama, 2004), Car-less *Rhodospirillum rubrum* LH1 can be obtained by exogenous recombination (Parkes-Loach, Sprinkle, & Loach, 1988). In the carotenoid-less *Rba. sphaeroides* mutant strain R26, the polymerized form of RC-LH is predominantly monomeric, and the curvature of the photosynthetic membrane is altered due to the lack of dimeric RC-LH (Ng et al., 2011). This implies that Cars assembly can regulate the conformation of the RC-LH complex. In our study, although the extensive interactions between subunit X, c-TM and LHαβ15 & LHαβ1 were disrupted in dRC-LH (Figures 2I and 4C), the correlation between Car depletion and the absence of subunit X has not been adequately verified. Since DPA treatment is not a clean way to examine the effect of Cars, it left several interior Cars still bound to the LH ring. DPA is a broad-spectrum inhibitor that slows cellular metabolic processes and specifically affects Car biosynthesis by inhibiting phytoene desaturase (CrtI), an essential enzyme catalyzes conversion of the colorless Car precursor phytoene to the colored lycopene (Bramley, 1993). We here found that DPA treatment not only dramatically decreased the *R. castenholzii* proliferation rate but also depleted the LH-bound Cars in dRC-LH (Figures 1A and 4, Figure 1—figure supplement 1B). Although DPA treatment did not strikingly affect cell proliferation grown under

2,000 lux and 100 lux light intensities, it still decreased the Car absorbance of the extracted dRC-LH (Figure 1—figure supplement 1E). Therefore, an efficient genetic manipulation system of *R. castenholzii* is required for elucidating the correlations between Cars and the RC-LH assembly, as well as the photosynthetic growth of cells.

In summary, this study revealed conformational changes of the *R. castenholzii* RC-LH in the presence and absence of $K\gamma C_{ext}$ and subunit X, which played an important role in regulating the conformation and quinone/quinol exchange rates. $K\gamma C_{ext}$ incorporation results in a sealed conformation of the LH ring, whereas Car depletion and absence of the subunit X produces an exposed LH ring with larger opening, which together accelerate the quinone/quinol exchange rate. These results demonstrate a correlation between LH-bound Cars and the assembly and quinone/quinol exchange of *R. castenholzii* RC-LH. Overall, these findings deepen our understanding of the light absorption and photo-reaction mechanisms in prokaryotic photosynthesis and increase the feasibility of applying prokaryotic photosystems in synthetic microbiology approaches.

Materials and methods

Extraction and purification of the RC-LH complexes from *Roseiflexus castenholzii*

The *Roseiflexus castenholzii* cells (strain DSM 13941/HLO8) were grown anaerobically at 50 ℃ under 10,000 lux, 2,000 lux and 100 lux light intensities in a modified PE medium as previously reported (Hanada, Takaichi, Matsuura, & Nakamura, 2002). To inhibit carotenoid biosynthesis, diphenylamine (DPA) was added to the medium (12 mg L^{-1}), and the bacteria were cultured under the same conditions as the native bacteria. Growth curves of the native and DPA-treated *R. castenholzii* cells were monitored with a UV–vis spectrophotometer (Mapada P6, Shanghai), by recording the absorption of cultured cells at 660 nm for every 12 hours. The mean values of the optical density at each time point and the standard deviations of mean (n=3) were calculated.

Isolation and purification of both the nRC-LH and dRC-LH complexes were carried out as described (Collins et al., 2009) with some modifications. The whole membranes (OD=20 cm^{-1} measured at 880 nm) in 20 mM Tris-HCl (pH 8.0) were solubilized by 0.45 % (w/v) β-DDM at room temperature for 1 hour with gentle stirring and then were ultra-centrifuged at 200,000 ×g for 1 hour. The supernatant was collected and filtered through a 0.22 μm filter and diluted with buffer A (0.04 % DDM, 50 mM Tris-HCl, pH 8.0), subsequently loaded on an anion exchange chromatography column (HiTrap Q HP, Cytiva, USA) that had been equilibrated with buffer A. The crude RC-LH complex was eluted from the column with 200 mM NaCl in buffer A, and further purified by gel filtration through a Superdex 200 16/600 column, and a Superose 6 Increase 10/300 GL (Cytiva, USA) in buffer B (0.04 % DDM, 100 mM NaCl, 50 mM Tris-HCl, pH 8.0). The whole preparation procedure was monitored by detecting the absorption spectrum from 250 to 900 nm.

HPLC-MS analyses of the pigments in RC-LH complexes

Pigment composition was analyzed by High performance liquid chromatography (HPLC) as described (Collins et al., 2009) The RC-LH samples were mixed with acetone / methanol (v / v ratio of 7:2) to extract the pigments, followed by centrifugation at 12,000 ×g for 15 min. Then the supernatant was filtered through a 0.22 μm filter membrane. The filtrate was injected into a C18 reversed-phase column (4.6 mm×150 mm, 5 μm particle size, Agilent, USA) in a Thermo-Fisher Ultimate 3000 separation module equipped with a DAD-3000 Diode Array Detector. The pigments were eluted at a flow rate of 1 mL min^{-1} using 100% methanol. Pigments were then detected by their absorbance at 442 nm and 772 nm. The commercial BChl *a* and γ-carotene (Sigma-Aldrich) were used as standards. Pigments were identified based on their absorption spectra, retention times and further analyzed by LC-MS. LC-MS was equipped with an Agilent 1200 HPLC system (Agilent, Santa Clara, CA. USA) and a Thermo Finnigan LCQDeca XP Max LC/MS system (Thermo Finnigan, Waltham, MA, USA). The condition of HPLC is the same as

the above. MS with an atmospheric pressure chemical ionization (APCI) source was performed as follows: positive mode, source voltage of 2.5 kV, capillary voltage of 46 V, sheath gas flow of 60 arbitrary units, auxiliary/sweep gas flow of 10 arbitrary units, capillary temperature 150 ℃. The pigments composition was determined as shown in Figure S9.

Cryo-electron microscopy

Three μL aliquots of the purified RC-LH (native and carotenoid depleted) complexes were placed on glow-discharged CryoMatrix R1.2/1.3 300-mesh amorphous alloy film (product no. M024-Au300-R12/13, Zhenjiang Lehua Technology Co. Ltd., China). Each grid was blotted for 3 s at 4 ℃ in 100 % humidity, then plunged into liquid ethane with a Mark IV Vitrobot system (Thermo Fisher Scientific, USA).

Data for the native RC-LH (nRC-LH) complex was collected on a 300 kV Titan Krios electron microscope (Thermo Fisher Scientific, USA) with a K3 direct electron detector (Gatan, USA) in counting mode. A total of 2,836 movies were recorded at a magnification of ×64,000 and a pixel size of 1.08 Å, with a total dose of approximately 50 e^{-} $Å^{-2}$, and a defocus range between -1.0 and -2.3 μm. Each movie was collected over 2.59 s and dose-fractionated into 40 frames. Data for the carotenoid depleted RC-LH (dRC-LH) complex was recorded on a 300 kV Titan Krios electron microscope with a K3 direct electron detector in counting mode. A nominal magnification of 81,000 ×was used for imaging, which yielded a pixel size of 0.893 Å. A total of 3,514 movies were collected with defocus values between -1.1 and -1.7μm. Each movie was dose-fractionated to 40 frames under a total dose rate of 49.65 e^{-} $Å^{-2}$ and an exposure time of 2.2 s. Cryo-EM analyses of nRC-LH complexes extracted from cells grown under 2,000 lux and 100 lux were summarized in Figure 1—figure supplement 3 and Table 2.

Image processing

Beam-induced motion correction and exposure weighting were performed by MotionCorr2 (Zheng et al., 2017), and the CTF (contrast transfer function) was estimated using the Gctf

program (Zhang, 2016). The automatic particle picking was performed by Gautomatch (developed by K. Zhang, https://www.mrc-lmb.cam.ac.uk/kzhang/Gautomatch/) and RELION. All other steps were performed using RELION 3.1 (Zivanov et al., 2018).

For the dataset of native RC-LH (nRC-LH) complex extracted from cells grown under 10,000 lux, the templates for automatic particle picking were 2D class averages of manually picked 3,106 particles. In total, 1,625,156 particles were auto-picked from 2,836 micrographs. The picked particles were extracted at 4 ×4 binning and subjected to two rounds of 2D classification. Good 2D class averages in different orientations were selected to generate the initial model. A subset of 1,041,360 particles at the original pixel size were selected for 3D classification into three classes with the initial model as a reference, and then 372,029 good particles were refined into a 3.7-Å resolution electron density map. Finally, the resultant data refined by per-particle CTF refinement were subjected to 3D refinement and postprocessing to 2.8 Å resolution on the gold-standard FSC (Fourier Shell Correlation) = 0.143 criterion. The image processing of nRC-LH complexes extracted from cells grown under 2,000 lux and 100 lux were summarized in Figure 1—figure supplement 3.

For the dataset of carotenoid depleted RC-LH (dRC-LH) complex, a total of 1,081,719 particles were automatically picked from 3,514 micrographs. The picked particles were extracted at 4 ×4 binning and subjected to three rounds of reference-free 2D classification, resulting in 191,821 particles being left and re-extracted into the original pixel size of 0.893 Å. After 3D classification with three classes of particles, a subset of 84,352 particles was selected for the final refinement and postprocessing. The resolution of the final map was 3.5 Å. The values of the angular distribution of particles from 3D refinement were visualized by ChimeraX (Pettersen et al., 2021). Local resolution was estimated with Resmap (Kucukelbir, Sigworth, & Tagare, 2014).

Model building and refinement

The reported 4.1-Å resolution model of RC-LH complex from *Roseiflexus castenholzii* (PDB ID: 5YQ7) (Xin et al., 2018) was fitted into the density map in ChimeraX. Based on the density map, the structural model of the native RC-LH (nRC-LH) complex, including the amino acids residues, cofactors, lipids and the newly identified exterior keto-γ-carotene ($K\gamma C_{ext}$ and KγC) molecules were manually built and adjusted in Coot (Emsley & Cowtan, 2004). Then real-space refinement in PHENIX (Adams et al., 2010) was used for model refinement with intra-cofactor and protein-cofactor geometric constraints. The structure of the carotenoid depleted RC-LH (dRC-LH) complex was also manually built using the refined model of nRC-LH as a reference in COOT (Emsley & Cowtan, 2004) and refined using the real-space refinement in PHENIX (Adams et al., 2010). The refinement and model statistics are listed in Table 2.

Assignment of the subunit X, proteins Y and Z

The Cryo-EM Map of nRC-LH was used for automated model building in ModelAngelo, a program developed by Professor Sjors Scheres (https://arxiv.org/abs/2210.00006v1). BLAST search of the deduced amino acid sequences of subunit X generated a hint with hypothetical protein KatS3mg058_1126 (GenBank: GIV99722.1) from *Roseiflexus sp.*, which was denoted by metagenomic analyses of the uncultivated bacteria in Katase hot spring sediment (Kato et al., 2022). However, this polypeptide has not been annotated in the Protein Database of *R. castenholzii* (strain DSM 13941/HLO8). By searching the genomic DNA of *R. castenholzii* (strain DSM 13941/HLO8), we eventually identified the coding sequences (CDS: 1,060,366-1,060,464) of subunit X, which shared strictly conserved amino acid sequence with KatS3mg058_1126. The assigned amino acid residues fitted well with the cryo-EM densities as shown in Figure 2H. Assignment of protein Y and Z was performed in same procedure, except that protein Z was also confirmed by PMF analyses shown in Table 1.

Steady-state and fluorescence spectroscopy

Absorption spectra of the RC-LH complexes were collected at wavelength ranging from 250 to 900 nm using a UV–vis spectrophotometer (Mapada P6, Shanghai). Fluorescence emission and excitation spectra of the nRC-LH and dRC-LH complexes were recorded using a steady-state and time-resolved Photoluminescence Spectrometer (Edinburgh FLS1000, UK), equipped with a Hamamatsu NIR PMT detector (Hamamatsu Photonics, Japan) and an external adjustable 980 nm continuous-wave (CW) laser. The fluorescence excitation spectra were obtained with emissions monitored at 920 nm, and excitation at 470 nm was used for emission spectra.

Auracyanin oxidation assays

Isolation and purification of endogenous auracyanin (Ac) from *Roseiflexus castenholzii* was carried out by the methods as described (Wang et al., 2020). Before the oxidation assay, the purified Ac was treated with sodium dithionite to obtain the reduced Ac. Using the reduced Ac (122 μM) as electron donor and varied concentrations of menaquinone-4 as electron acceptor, the reaction was carried out in presence of nRC-LH or dRC-LH complex (50 nM) in buffer B (0.04 % DDM, 100 mM NaCl, 50 mM Tris-HCl, pH 8.0). The reaction was initiated by illumination at 10,000 lux light intensity, and the absorbance of Ac at 604 nm was recorded by a UV–vis spectrophotometer (Mapada P6, Shanghai) at 2 min intervals for a total of 14 min. The corresponding concentrations of Ac were calculated with extinction coefficient, and linear initial rates from 2 to 14 min were fitted using the Michaelis-Menten model in Prism8. All data were obtained from three replicative experiments, with the mean and standard deviations calculated and plotted.

Data availability: Cryo-EM maps and atomic coordinates of the native RC-LH (nRC-LH) and carotenoid depleted RC-LH (dRC-LH) complexes extracted from cells grown under 10,000 lux light intensity have been deposited into the Electron Microscopy Data Bank (accession codes, EMD-34838 and EMD-34839) and the Protein Data Bank (PDB) (accession codes, 8HJU and 8HJV), respectively. Cryo-EM maps and atomic coordinates of the nRC-LH complexes

extracted from cells grown under 100 lux and 2,000 lux have been deposited into the Electron Microscopy Data Bank (accession codes, EMD-35988 and EMD-35989) and the Protein Data Bank (PDB) (accession codes, 8J5O and 8J5P), respectively. Cryo-EM maps and atomic coordinates of the four RC-LH complexes can also be accessed at this URL: https://datadryad.org/stash/share/4qsqf_fvShvTvqfPZzXDdP3_uEEknnWJAEOxdxV6XrY. Other data are available from the corresponding authors upon reasonable request.

References

Adams, P. D., Afonine, P. V., Bunkoczi, G., Chen, V. B., Davis, I. W., Echols, N., Headd, J. J., Hung, L. W., Kapral, G. J., Grosse-Kunstleve, R. W., McCoy, A. J., Moriarty, N. W., Oeffner, R., Read, R. J., Richardson, D. C., Richardson, J. S., Terwilliger, T. C., & Zwart, P. H. (2010). PHENIX: a comprehensive Python-based system for macromolecular structure solution. *Acta Crystallogr D Biol Crystallogr, 66*(Pt 2), 213-221. doi:10.1107/S0907444909052925

Bramley, P. (1993). Inhibition of carotenoid biosynthesis. In *Carotenoids in photosynthesis* (pp. 127-159): Springer.

Cao, P., Bracun, L., Yamagata, A., Christianson, B. M., Negami, T., Zou, B., Terada, T., Canniffe, D. P., Shirouzu, M., Li, M., & Liu, L. N. (2022). Structural basis for the assembly and quinone transport mechanisms of the dimeric photosynthetic RC-LH1 supercomplex. *Nat Commun, 13*(1), 1977. doi:10.1038/s41467-022-29563-3

Collins, A. M., Qian, P., Tang, Q., Bocian, D. F., Hunter, C. N., & Blankenship, R. E. (2010). Light-harvesting antenna system from the phototrophic bacterium Roseiflexus castenholzii. *Biochemistry, 49*(35), 7524-7531. doi:10.1021/bi101036t

Collins, A. M., Xin, Y., & Blankenship, R. E. (2009). Pigment organization in the photosynthetic apparatus of Roseiflexus castenholzii. *Biochim Biophys Acta, 1787*(8), 1050-1056. doi:10.1016/j.bbabio.2009.02.027

Davidson, E., & Cogdell, R. J. (1981). Reconstitution of carotenoids into the light-harvesting pigment-protein complex from the carotenoidless mutant of Rhodopseudomonas as sphaeroides R26. *Biochim Biophys Acta, 635*(2), 295-303. doi:10.1016/0005-2728(81)90028-1

Emsley, P., & Cowtan, K. (2004). Coot: model-building tools for molecular graphics. *Acta Crystallogr D Biol Crystallogr, 60*(Pt 12 Pt 1), 2126-2132. doi:10.1107/S0907444904019158

Fiedor, L., Akahane, J., & Koyama, Y. (2004). Carotenoid-induced cooperative formation of bacterial photosynthetic LH1 complex. *Biochemistry, 43*(51), 16487-16496. doi:10.1021/bi0481287

Gall, A., Henry, S., Takaichi, S., Robert, B., & Cogdell, R. J. (2005). Preferential incorporation of coloured-carotenoids occurs in the LH2 complexes from non-sulphur purple bacteria under carotenoid-limiting conditions. *Photosynth Res, 86*(1-2), 25-35. doi:10.1007/s11120-005-3481-0

Hanada, S., Takaichi, S., Matsuura, K., & Nakamura, K. (2002). Roseiflexus castenholzii gen. nov., sp. nov., a thermophilic, filamentous, photosynthetic bacterium that lacks chlorosomes. *Int J Syst Evol Microbiol, 52*(Pt 1), 187-193. doi:10.1099/00207713-52-1-187

Hashimoto, H., Uragami, C., & Cogdell, R. J. (2016). Carotenoids and Photosynthesis. *Subcell Biochem, 79*, 111-139. doi:10.1007/978-3-319-39126-7_4

Jackson, P. J., Hitchcock, A., Swainsbury, D. J. K., Qian, P., Martin, E. C., Farmer, D. A., Dickman, M. J., Canniffe, D. P., & Hunter, C. N. (2018). Identification of protein W, the elusive sixth subunit of the Rhodopseudomonas palustris reaction center-light harvesting 1 core complex. *Biochim Biophys Acta Bioenerg, 1859*(2), 119-128. doi:10.1016/j.bbabio.2017.11.001

Kato, S., Masuda, S., Shibata, A., Shirasu, K., & Ohkuma, M. (2022). Insights into ecological roles of uncultivated bacteria in Katase hot spring sediment from long-read metagenomics. *Front Microbiol, 13*, 1045931. doi:10.3389/fmicb.2022.1045931

Kishi, R., Imanishi, M., Kobayashi, M., Takenaka, S., Madigan, M. T., Wang-Otomo, Z. Y., & Kimura, Y. (2021). Quinone transport in the closed light-harvesting 1 reaction center complex from the thermophilic purple bacterium Thermochromatium tepidum. *Biochim Biophys Acta Bioenerg, 1862*(1), 148307. doi:10.1016/j.bbabio.2020.148307

Kucukelbir, A., Sigworth, F. J., & Tagare, H. D. (2014). Quantifying the local resolution of cryo-EM density maps. *Nat Methods, 11*(1), 63-65. doi:10.1038/nmeth.2727

Lang, H., & Hunter, C. N. J. B. J. (1994). The relationship between carotenoid biosynthesis and the assembly of the light-harvesting LH2 complex in Rhodobacter sphaeroides. *298*(1), 197-205.

Lang, H. P., Cogdell, R. J., Takaichi, S., & Hunter, C. N. (1995). Complete DNA sequence, specific Tn5 insertion map, and gene assignment of the carotenoid biosynthesis pathway of Rhodobacter sphaeroides. *J Bacteriol, 177*(8), 2064-2073. doi:10.1128/jb.177.8.2064-2073.1995

McGlynn, P., Hunter, C. N., & Jones, M. R. (1994). The Rhodobacter sphaeroides PufX protein is not required for photosynthetic competence in the absence of a light harvesting system. *FEBS Lett, 349*(3), 349-353. doi:10.1016/0014-5793(94)00701-2

Ng, I. W., Adams, P. G., Mothersole, D. J., Vasilev, C., Martin, E. C., Lang, H. P., Tucker, J. D., & Neil Hunter, C. (2011). Carotenoids are essential for normal levels of dimerisation of the RC-LH1-PufX core complex of Rhodobacter sphaeroides: characterisation of R-26 as a crtB (phytoene synthase) mutant. *Biochim Biophys Acta, 1807*(9), 1056-1063. doi:10.1016/j.bbabio.2011.05.020

Niwa, S., Yu, L. J., Takeda, K., Hirano, Y., Kawakami, T., Wang-Otomo, Z. Y., & Miki, K. (2014). Structure of the LH1-RC complex from Thermochromatium tepidum at 3.0 A. *Nature, 508*(7495), 228-232. doi:10.1038/nature13197

Olsen, J. D., Martin, E. C., & Hunter, C. N. (2017). The PufX quinone channel enables the light-harvesting 1 antenna to bind more carotenoids for light collection and photoprotection. *FEBS Lett, 591*(4), 573-580. doi:10.1002/1873-3468.12575

Parkes-Loach, P. S., Sprinkle, J. R., & Loach, P. A. (1988). Reconstitution of the B873 light-harvesting complex of Rhodospirillum rubrum from the separately isolated alpha- and beta-polypeptides and bacteriochlorophyll a. *Biochemistry, 27*(8), 2718-2727. doi:10.1021/bi00408a011

Pettersen, E. F., Goddard, T. D., Huang, C. C., Meng, E. C., Couch, G. S., Croll, T. I., Morris, J. H., & Ferrin, T. E. (2021). UCSF ChimeraX: Structure visualization for researchers, educators, and developers. *Protein Sci, 30*(1), 70-82. doi:10.1002/pro.3943

Polivka, T., & Frank, H. A. (2010). Molecular factors controlling photosynthetic light harvesting by carotenoids. *Acc Chem Res, 43*(8), 1125-1134. doi:10.1021/ar100030m

Pugh, R. J., McGlynn, P., Jones, M. R., & Hunter, C. N. (1998). The LH1-RC core complex of Rhodobacter sphaeroides: interaction between components, time-dependent assembly, and topology of the PufX protein. *Biochim Biophys Acta, 1366*(3), 301-316. doi:10.1016/s0005-2728(98)00131-5

Qian, P., Croll, T. I., Swainsbury, D. J. K., Castro-Hartmann, P., Moriarty, N. W., Sader, K., & Hunter, C. N. (2021). Cryo-EM structure of the Rhodospirillum rubrum RC-LH1 complex at 2.5 A. *Biochem J, 478*(17), 3253-3263. doi:10.1042/BCJ20210511

Qian, P., Gardiner, A. T., Simova, I., Naydenova, K., Croll, T. I., Jackson, P. J., Nupur, Kloz, M., Cubakova, P., Kuzma, M., Zeng, Y., Castro-Hartmann, P., van Knippenberg, B., Goldie, K. N., Kaftan, D., Hrouzek, P., Hajek, J., Agirre, J., Siebert, C. A., Bina, D., Sader, K., Stahlberg, H., Sobotka, R., Russo, C. J., Polivka, T., Hunter, C. N., & Koblizek, M. (2022). 2.4-A structure of the double-ring Gemmatimonas phototrophica photosystem. *Sci Adv, 8*(7), eabk3139. doi:10.1126/sciadv.abk3139

Qian, P., Hunter, C. N., & Bullough, P. A. (2005). The 8.5A projection structure of the core RC-LH1-PufX dimer of Rhodobacter sphaeroides. *J Mol Biol, 349*(5), 948-960. doi:10.1016/j.jmb.2005.04.032

Qian, P., Siebert, C. A., Wang, P., Canniffe, D. P., & Hunter, C. N. (2018). Cryo-EM structure of the Blastochloris viridis LH1-RC complex at 2.9 A. *Nature, 556*(7700), 203-208. doi:10.1038/s41586-018-0014-5

Qian, P., Swainsbury, D. J. K., Croll, T. I., Castro-Hartmann, P., Divitini, G., Sader, K., & Hunter, C. N. (2021). Cryo-EM Structure of the Rhodobacter sphaeroides Light-Harvesting 2 Complex at 2.1 A. *Biochemistry, 60*(44), 3302-3314. doi:10.1021/acs.biochem.1c00576

Qian, P., Swainsbury, D. J. K., Croll, T. I., Salisbury, J. H., Martin, E. C., Jackson, P. J., Hitchcock, A., Castro-Hartmann, P., Sader, K., & Hunter, C. N. (2021). Cryo-EM structure of the monomeric Rhodobacter sphaeroides RC-LH1 core complex at 2.5 A. *Biochem J, 478*(20), 3775-3790. doi:10.1042/BCJ20210631

Sener, M., Strumpfer, J., Hsin, J., Chandler, D., Scheuring, S., Hunter, C. N., & Schulten, K. (2011). Forster energy transfer theory as reflected in the structures of photosynthetic light-harvesting systems. *Chemphyschem, 12*(3), 518-531. doi:10.1002/cphc.201000944

Swainsbury, D. J. K., Qian, P., Jackson, P. J., Faries, K. M., Niedzwiedzki, D. M., Martin, E. C., Farmer, D. A., Malone, L. A., Thompson, R. F., Ranson, N. A., Canniffe, D. P., Dickman, M. J., Holten, D., Kirmaier, C., Hitchcock, A., & Hunter, C. N. (2021). Structures of Rhodopseudomonas palustris RC-LH1 complexes with open or closed quinone channels. *Sci Adv, 7*(3). doi:10.1126/sciadv.abe2631

Tani, K., Kanno, R., Ji, X. C., Hall, M., Yu, L. J., Kimura, Y., Madigan, M. T., Mizoguchi, A., Humbel, B. M., & Wang-Otomo, Z. Y. (2021). Cryo-EM Structure of the Photosynthetic LH1-RC Complex from Rhodospirillum rubrum. *Biochemistry*. doi:10.1021/acs.biochem.1c00360

Tani, K., Kanno, R., Kikuchi, R., Kawamura, S., Nagashima, K. V. P., Hall, M., Takahashi, A., Yu, L. J., Kimura, Y., Madigan, M. T., Mizoguchi, A., Humbel, B. M., & Wang-Otomo, Z. Y. (2022). Asymmetric structure of the native Rhodobacter sphaeroides dimeric LH1-RC complex. *Nat Commun, 13*(1), 1904. doi:10.1038/s41467-022-29453-8

Tani, K., Kanno, R., Kurosawa, K., Takaichi, S., Nagashima, K. V. P., Hall, M., Yu, L. J., Kimura, Y., Madigan, M. T., Mizoguchi, A., Humbel, B. M., & Wang-Otomo, Z. Y. (2022). An LH1-RC photocomplex from an extremophilic phototroph provides insight into origins of two photosynthesis proteins. *Commun Biol, 5*(1), 1197. doi:10.1038/s42003-022-04174-2

Tani, K., Nagashima, K. V. P., Kanno, R., Kawamura, S., Kikuchi, R., Hall, M., Yu, L. J., Kimura, Y., Madigan, M. T., Mizoguchi, A., Humbel, B. M., & Wang-Otomo, Z. Y. (2021). A previously unrecognized membrane protein in the Rhodobacter sphaeroides LH1-RC photocomplex. *Nat Commun, 12*(1), 6300. doi:10.1038/s41467-021-26561-9

Walz, T., & Ghosh, R. (1997). Two-dimensional crystallization of the light-harvesting I-reaction centre photounit from Rhodospirillum rubrum. *J Mol Biol, 265*(2), 107-111. doi:10.1006/jmbi.1996.0714

Wang, C., Xin, Y., Min, Z., Qi, J., Zhang, C., & Xu, X. (2020). Structural basis underlying the electron transfer features of a blue copper protein auracyanin from the photosynthetic bacterium Roseiflexus castenholzii. *Photosynth Res, 143*(3), 301-314. doi:10.1007/s11120-020-00709-y

Xin, Y., Pan, J., Collins, A. M., Lin, S., & Blankenship, R. E. (2012). Excitation energy transfer and trapping dynamics in the core complex of the filamentous photosynthetic bacterium Roseiflexus castenholzii. *Photosynth Res, 111*(1-2), 149-156. doi:10.1007/s11120-011-9669-6

Xin, Y., Shi, Y., Niu, T., Wang, Q., Niu, W., Huang, X., Ding, W., Yang, L., Blankenship, R. E., Xu, X., & Sun, F. (2018). Cryo-EM structure of the RC-LH core complex from an early branching photosynthetic prokaryote. *Nat Commun, 9*(1), 1568. doi:10.1038/s41467-018-03881-x

Yamada, M., Zhang, H., Hanada, S., Nagashima, K. V., Shimada, K., & Matsuura, K. (2005). Structural and spectroscopic properties of a reaction center complex from the chlorosome-lacking filamentous anoxygenic phototrophic bacterium Roseiflexus castenholzii. *J Bacteriol, 187*(5), 1702-1709. doi:10.1128/JB.187.5.1702-1709.2005

Yu, L. J., Suga, M., Wang-Otomo, Z. Y., & Shen, J. R. (2018a). Novel features of LH1-RC from Thermochromatium tepidum revealed from its atomic resolution structure. *FEBS J, 285*(23), 4359-4366. doi:10.1111/febs.14679

Yu, L. J., Suga, M., Wang-Otomo, Z. Y., & Shen, J. R. (2018b). Structure of photosynthetic LH1-RC supercomplex at 1.9 A resolution. *Nature, 556*(7700), 209-213. doi:10.1038/s41586-018-0002-9

Zhang, K. (2016). Gctf: Real-time CTF determination and correction. *J Struct Biol, 193*(1), 1-12. doi:10.1016/j.jsb.2015.11.003

Zheng, S. Q., Palovcak, E., Armache, J. P., Verba, K. A., Cheng, Y., & Agard, D. A. (2017). MotionCor2: anisotropic correction of beam-induced motion for improved cryo-electron microscopy. *Nat Methods, 14*(4), 331-332. doi:10.1038/nmeth.4193

Zivanov, J., Nakane, T., Forsberg, B. O., Kimanius, D., Hagen, W. J., Lindahl, E., & Scheres, S. H. (2018). New tools for automated high-resolution cryo-EM structure determination in RELION-3. *Elife, 7*. doi:10.7554/eLife.42166

Acknowledgments

We thank Professor Fei Sun at the Institute of Biophysics, Chinese Academy of Science, and Professor Weimin Ma at Shanghai Normal University for helpful discussions. We thank Danyu Gu from the Instrumentation and Service Center for Molecular Sciences at Westlake University for the assistance in measurement and data interpretation of the steady-state spectroscopic analyses. We appreciate the help from Prof. Kezhi Jiang of Hangzhou Normal University for the HPLC analysis of pigments. We thank the staff members of the Electron Microscopy System at the National Facility for Protein Science in Shanghai (NFPS), Zhangjiang Lab, China for providing technical support and assistance in data collection of the carotenoid depleted RC-LH complex. We also thank Shuimu BioSciences Ltd. for the support of cryo-EM data collection for the native RC-LH complex.

Funding: This work was supported by grants from the National Natural Science Foundation of China (31870740, 32171227, 31570738), Zhejiang Provincial Natural Science Foundation of China under Grant No. LR22C020002 to X. L. X. and Zhejiang Provincial Education Department under Grant No. Y202044875 to J. Y. X.

Author contributions: X. L. X. initiated the project and supervised all experiments. J. Y. X. purified and determined the cryo-EM structures of both the native and carotenoid depleted RC-LH complexes from *Roseiflexus castenholzii*, and performed the steady-state spectroscopic analyses. Y. S. assigned the subunit X, protein Y and Z in the RC-LH complex. X. Z. assisted in cryo-EM sample preparation and data processing. X. Y. Y. and H. M. H. performed the HPLC and LC-MS analyses of the pigments. Y. Y. X. and J. J. S. assisted in the spectral and enzymatic characterizations of the RC-LH complexes. X. L. X., R. E. B and J. Y. X. analyzed the data and wrote the manuscript.

Competing interests: The authors declare no conflict of interest.

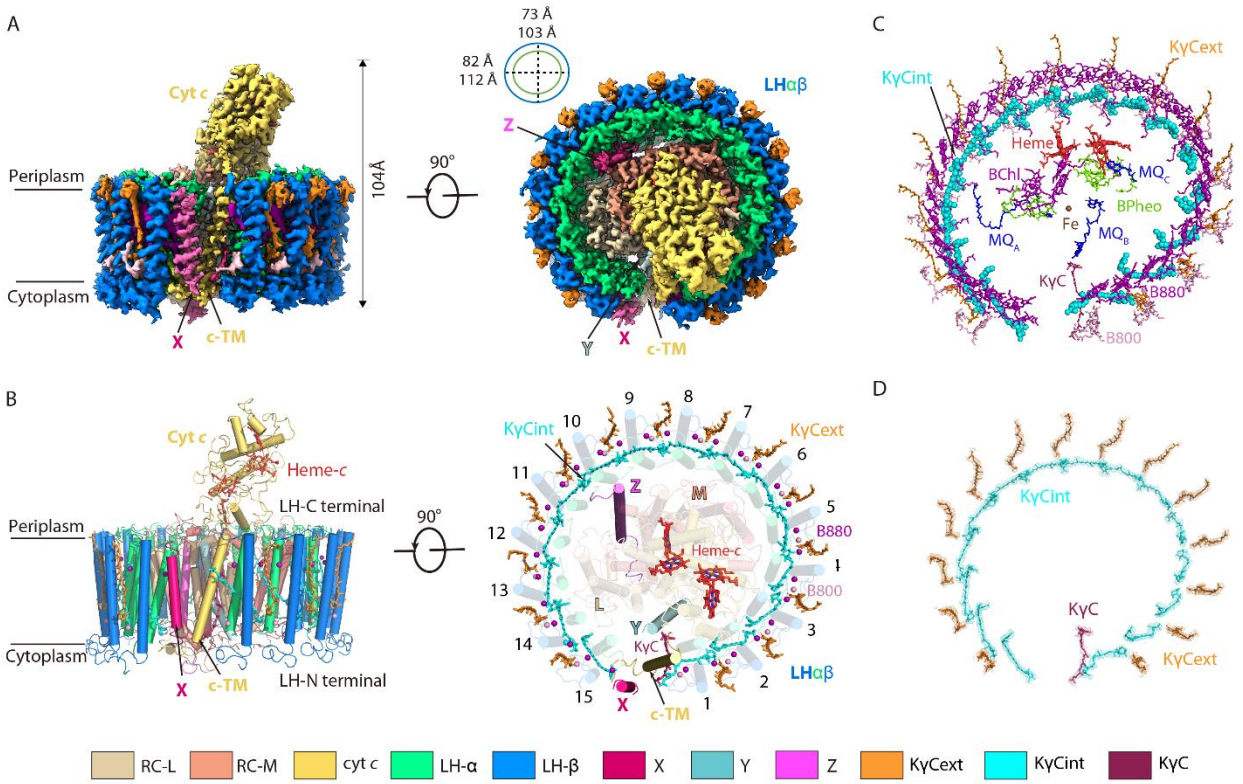

Figure 1. Overall structure of the native reaction center (RC)-light harvesting (LH) complex from *Roseiflexus castenholzii*. (A) A cryo-EM map of the native RC-LH (nRC-LH) complex is shown from the side (left panel) and the bottom (right panel). The dimensions of the RC-LH complex and LH ring are represented. The positions of subunit X, proteins Y and Z, and the cytochrome (cyt) *c* transmembrane domain (c-TM) are labeled. **(B)** Side and top views of the nRC-LH complex are presented in cartoon form. LH subunits are numbered clockwise from the gap formed by subunit X and c-TM. Heme-*c* (red) and keto-γ-carotene molecules (orange, cyan, ruby) are shown in stick forms; Mg atoms of the bacteriochlorophylls B800 (pink) and B880 (purple) are shown as spheres. **(C)** The cofactors bound in the nRC-LH complex. All cofactors are shown in stick forms except for the interior keto-γ-carotenes ($K\gamma C_{int}$) in LH, the iron bound in the RC are shown as spheres. **(D)** The structural models of the interior keto-γ-carotenes ($K\gamma C_{int}$), exterior keto-γ-carotenes ($K\gamma C_{ext}$) and KγC in the nRC-LH complex are fitted in the EM density map. The color scheme: Lime green, α-polypetides; marine, β-polypetides; yellow-orange, cyt *c*; wheat, L subunit; salmon, M subunit; pale cyan, protein Y; hot pink, subunit X;

light magenta, protein Z; cyan, KγC$_{int}$; orange, KγC$_{ext}$; ruby, KγC; Purple, B880; pink, B800; tv-red, heme-*c*; chartreuse, BPheos; blue, menaquinone-11 (MQ); brown, iron.

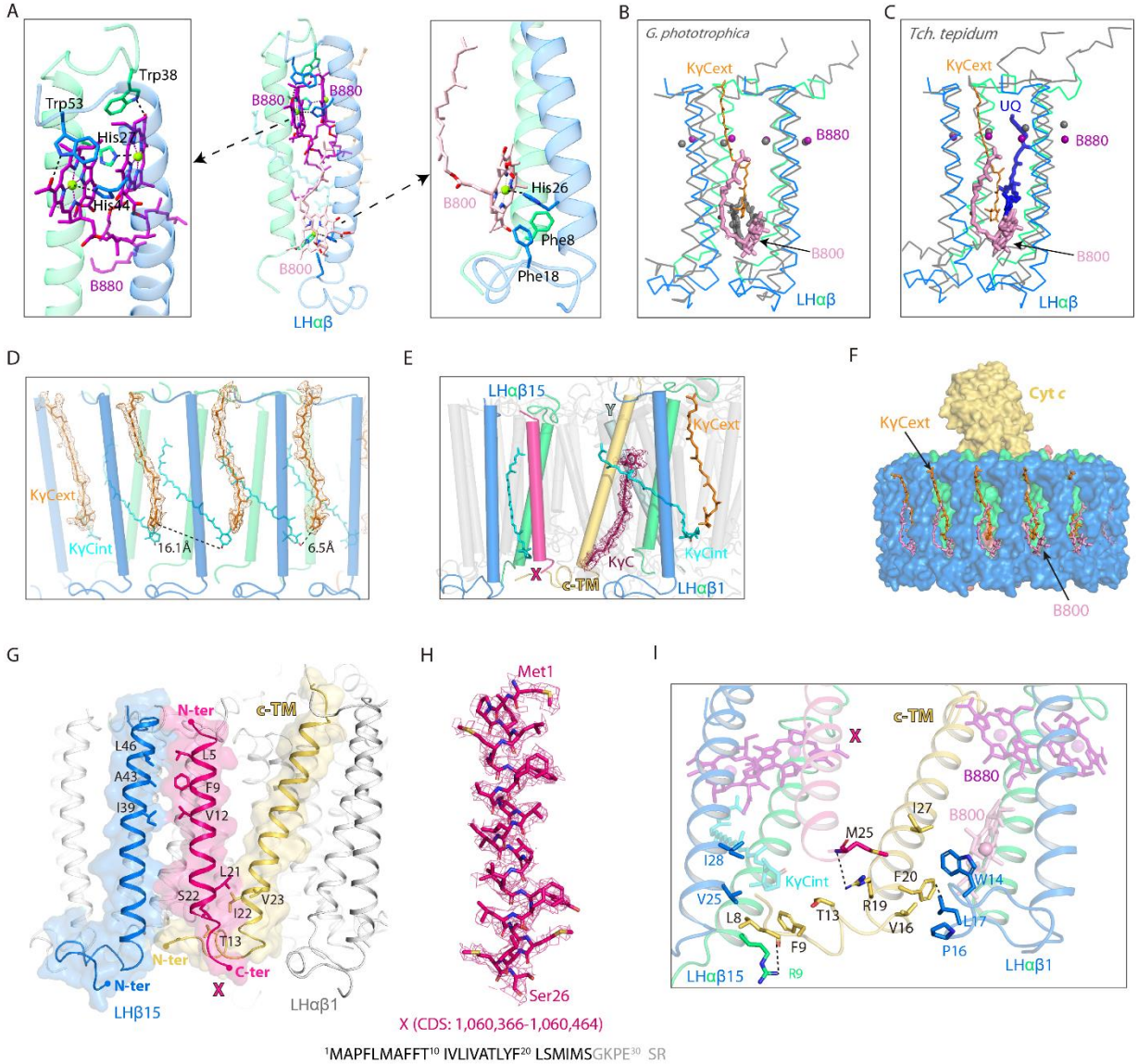

Figure 2. Interactions of the keto-γ-carotenes, BChls, and subunit X with the light harvesting (LH) ring. (A) Interactions between the LHαβ heterodimer and the bound BChls. Close-up views of amino acid residues that coordinate the LH-bound B880s (left) and B800 (right) are shown on the two sides. The BChls and interacting amino acid residues are shown in stick forms. **(B, C)** Superposition of LHαβ heterodimer from nRC-LH (colored) with *Gemmatimonas* (*G.*) *phototrophica* LHh (B, gray) and *Thermochromatium* (*Tch.*) *tepidum* LH1

(C, gray). The LH-bound B800 and exterior keto-γ-carotenes ($K\gamma C_{ext}$) in nRC-LH are shown as pink and orange sticks, respectively. Mg atoms of LH-bound B880 are shown in spheres. The LHh-bound B800 in *G. phototrophica* is shown in gray sticks, and *Tch. tepidum* LH1-bound ubiquinone (UQ) is shown in blue sticks. **(D, E)** Keto-γ-carotene organization. Interior keto-γ-carotenes ($K\gamma C_{int}$) are shown in cyan, exterior keto-γ-carotenes ($K\gamma C_{ext}$) are shown in orange, and the KγC inserted between c-TM and LHαβ is shown in ruby. **(F)** Incorporation of the $K\gamma C_{ext}$ and B800s at the cytoplasmic side blocked the LHαβ interface. **(G, I)** Interactions between the assigned subunit X (hot pink), c-TM (yellow-orange), and neighboring LHαβ1 and LHαβ15 in the nRC-LH. The N-terminus (N-ter) and C-terminus (C-ter) of subunit X, c-TM and LHβ15 are indicated. The hydrogen bonding and hydrophobic interactions between the amino acid residues are labeled and indicated with dashed lines. The BChls B880 and B800 are shown as purple and pink sticks, respectively. **(H)** The assigned subunit X (hot pink) are fitted in the EM density map. Location of the coding sequence (CDS) in *R. castenholzii* genomic DNA, and the amino acid sequence of subunit X are indicated, with the modeled amino acid residues colored in black.

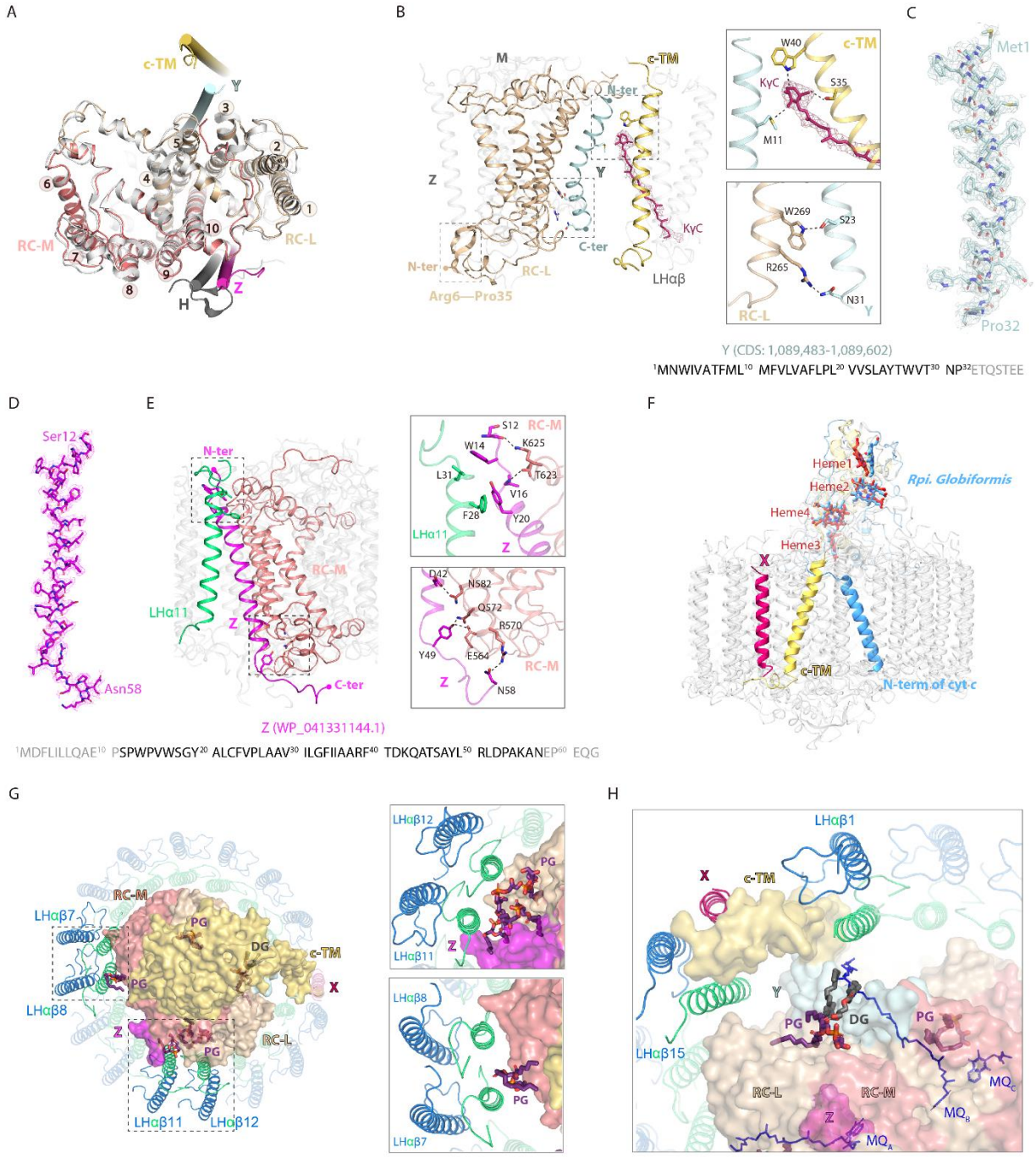

Figure 3. Stabilizing the reaction center (RC)-light harvesting (LH) interactions. (A) Superposition of R. castenholzii RC structure (colored) with that of Rhodobacter (Rba.) sphaeroides (white, PDB ID: 7F0L) showed excellent match at the L (wheat) and M (salmon) subunits, each of which contains five transmembrane helices (TM1-5 for L, and TM-6-10 for M). The newly assigned TM helices from protein Y (pale cyan) and Z (light magenta) are located on the two sides of the RC. The only TM helix of Rba. sphaeroides H subunit (gray) does

not match with that of protein Z. **(B)** Interactions between the assigned protein Y (pale cyan), c-TM (yellow-orange), and the RC-L (wheat). The N-terminus (N-ter) and C-terminus (C-ter) of Y, and RC-L N-terminal extension (Arg6-Pro35) are indicated. The hydrogen bonding interactions between the amino acid residues and KγC (ruby sticks) are labeled and indicated with dashed lines in the insects. **(C, D)** The assigned TM helix of protein Y (C, pale cyan) and protein Z (D, light magenta) are fitted in the EM density map. Location of the coding sequence (CDS) of Y in R. castenholzii genomic DNA, and the protein accession number of protein Z are indicated. The amino acid sequences of protein Y and Z are indicated below, with the modeled amino acid residues colored in black. **(E)** Interactions between the assigned protein Z (light magenta), LHα11 (lime green), and the RC-M (salmon). The N-terminus (N-ter) and C-terminus (C-ter) of Z are indicated. The hydrogen bonding interactions are shown in the insects. **(F)** Superposition of R. castenholzii RC-bound cyt c (yellow-orange) with that of Rhodopila (Rpi.) Globiformis (cornflower blue, PDB ID: 7XXF) showed excellent match at the tetra-heme binding domain. The c-TM and N-ter of Rpi. Globiformis cyt c directed into opposite directions. **(G, H)** Interactions of the lipids (phosphatidylglycerol, PG; and diglyceride, DG) with the LH and RC. The L, M and cyt c subunits of RC are shown in surface, and LHαβs are shown in cartoon forms, the lipids and RC-bound menaquinone-11s (MQs) are shown in deep purple and blue sticks, respectively.

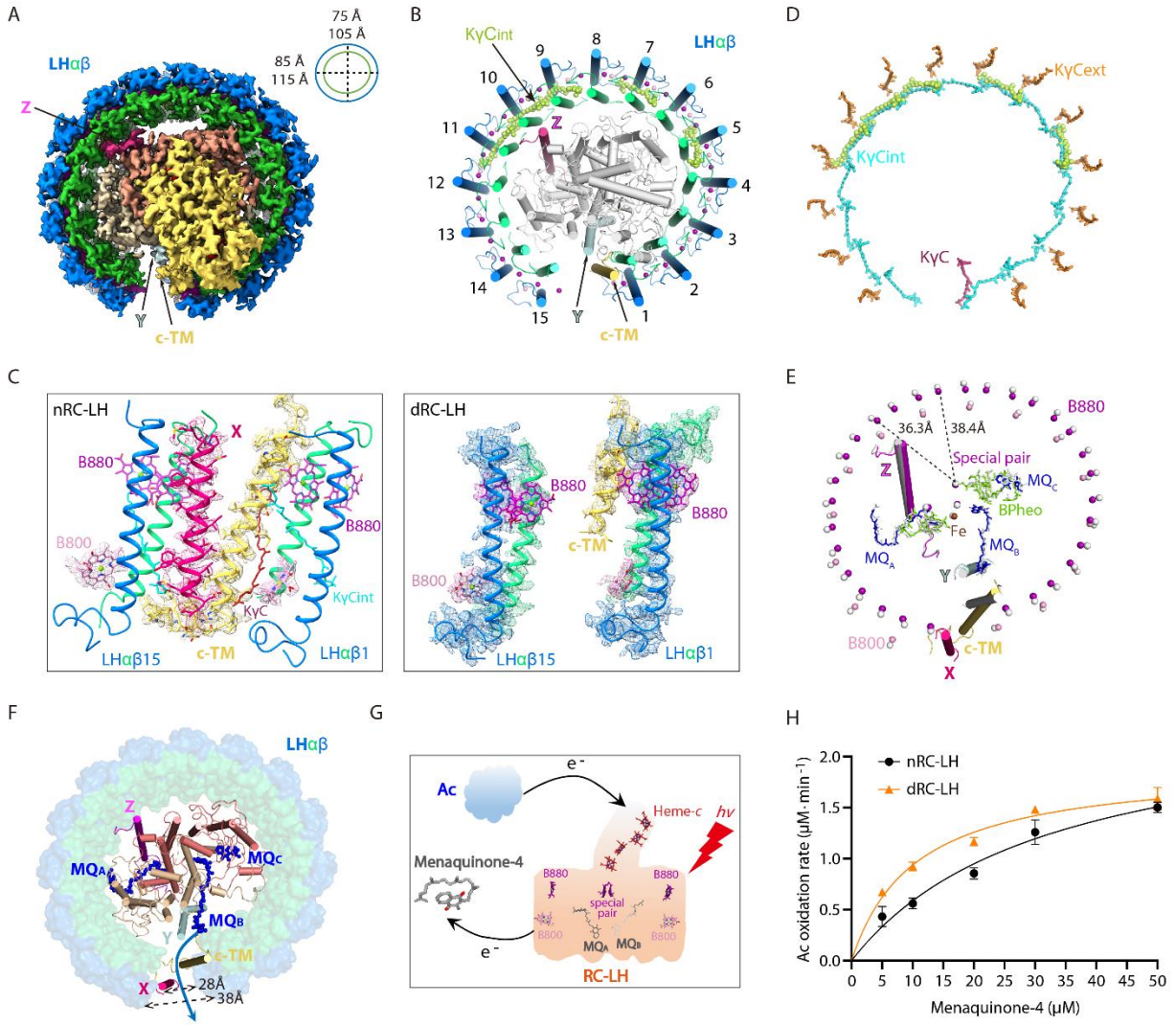

Figure 4. Cryo-EM structure of the carotenoid depleted reaction center-light harvesting (dRC-LH) complex of *Roseiflexus castenholzii* and its conformational changes that accelerated quinone/quinol exchange. (A) Cryo-EM map of dRC-LH seen from the bottom with LH ring dimensions indicated. **(B)** Cartoon representation of the dRC-LH complex from the bottom. The interior keto-γ-carotenes ($K\gamma C_{int}$) are shown in limon and bacteriochlorophyll (BChl) Mg atoms are shown as spheres. **(C)** Comparison of the LH ring openings in the nRC-LH (left) and dRC-LH (right). The cryo-EM maps of the subunit X (hot pink), c-TM (yellow-orange) and neighboring LHαβ1 and LHαβ15 are shown to indicate the conformational changes. The LH-bound B880s (purple), B800s (pink) and KγC (ruby) are shown in sticks and fitted in the EM map. **(D)** Comparison of the keto-γ-carotene arrangement between the nRC-LH and dRC-LH

complexes. The KγC$_{int}$, KγC$_{ext}$ and KγC in nRC-LH are shown as cyan, orange and ruby sticks, respectively. The five KγC$_{int}$ molecules bound in the dRC-LH complex are shown as limon spheres. **(E)** Comparison of the central BChl-Mg atoms in nRC-LH and dRC-LH. The B880 and B800 Mg atoms are shown as purple and pink spheres, respectively, in nRC-LH, and as white spheres in dRC-LH. The two structures are superposed at the TM helices of the L and M subunits. The distances between the central Mg atoms of B880 and the nearest special pair BChls are labeled and indicated with dashed lines. The cofactors bound in the RC are shown in stick form; the iron is shown as spheres. TM helices of Subunit X (hot pink), protein Y (pale cyan), Z (light magenta), c-TM (yellow-orange in nRC-LH and white in dRC-LH), and LH$\alpha\beta$1 and LH$\alpha\beta$15 (colored in nRC-LH and white in dRC-LH) are shown in ribbon form to demonstrate the spatial organization. **(F)** Comparison of the LH ring opening and quinone channels in nRC-LH and dRC-LH. The LH ring of dRC-LH is shown in surface form; the RC (including Y and Z), c-TM, and subunit X in nRC-LH are shown in cartoon forms; and menaquinones (MQs) are shown in blue sticks. Dashed lines indicate the dimensions of the LH ring openings in the two structures. The blue arrow represents the putative quinone shuttling path. **(G)** Model diagram of the auracyanin (Ac) oxidation assay. Upon illumination, light energy absorbed by the LH-bound BChls (B800 and B880) is transferred to RC. The primary charge separation occurs and initiates sequential electron transfer that reduces the MQs. The generated hydroquinone diffuses out of the RC-LH and exchanges with the menaquinone-4 in the solution. Once the reduced Ac is oxidized, the released electrons can be transferred back to reduce the photo-oxidized special pair through the *c*-type hemes. **(H)** The rate of auracyanin (Ac) oxidation at various starting concentrations of menaquinone-4, in presence of the nRC-LH (black) or dRC-LH (orange).

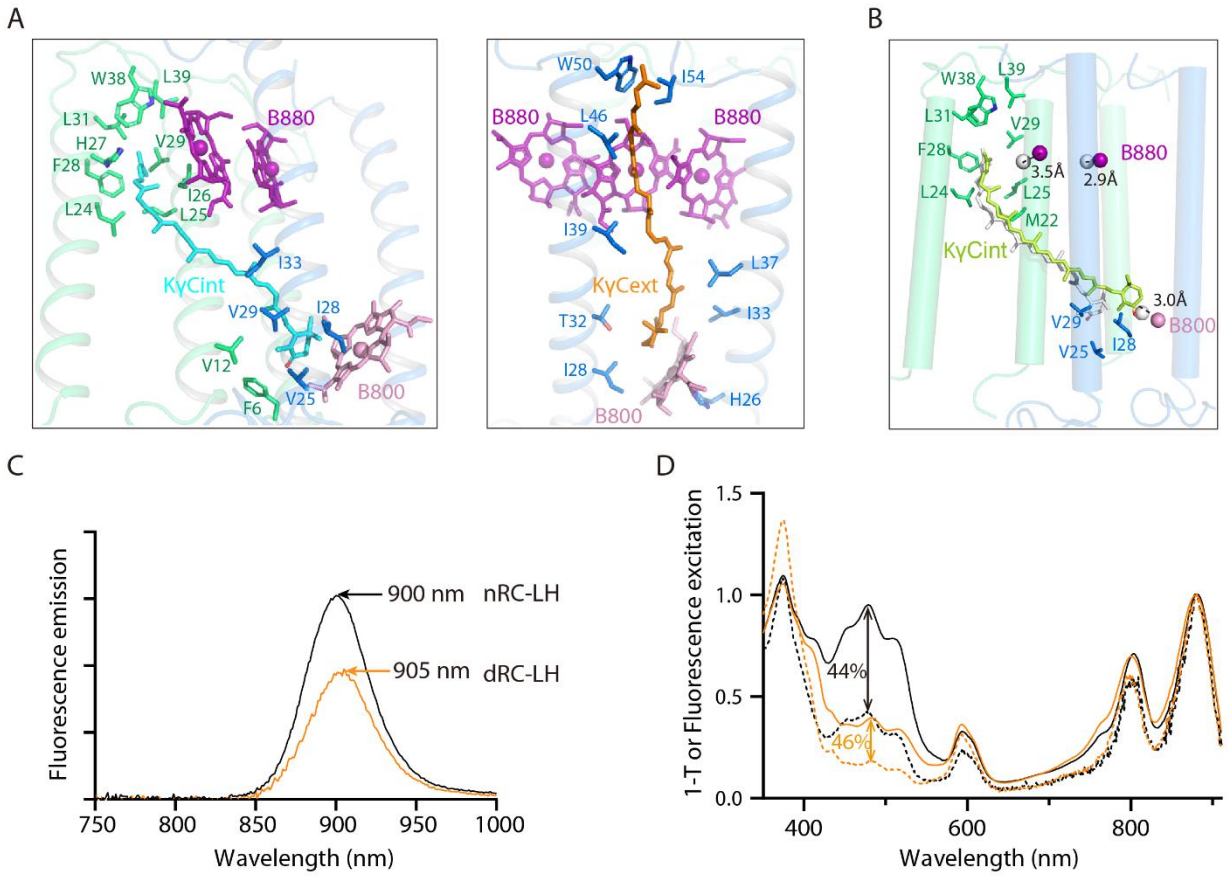

Figure 5. Binding conformation of the interior and exterior keto-γ-carotenes (KγC$_{int}$ and KγC$_{ext}$, respectively) and measurement of the Car-to-BChl energy transfer efficiency in nRC-LH and dRC-LH complexes. (A) Coordination of representative KγC$_{int}$ (cyan) and KγC$_{ext}$ (orange) molecules in the nRC-LH complex. Shown as stick forms are the amino acid residues from LHα (lime green) and LHβ (marine) surrounding the 4-oxo-β-ionone ring; the ψ-end group of the keto-γ-carotenes; and the BChls B880 (purple) and B800 (pink) in the nearby LHαβ. **(B)** Coordination of the KγC$_{int}$ molecules, which are shown in limon and white in dRC-LH and nRC-LH, respectively. Amino acid residues from the nearby LHα (lime green) and LHβ (marine) and the B800 molecule that covers the head and tail of this KγC$_{int}$ molecule are shown as stick forms. The distance deviations of the central Mg atoms in B880 (purple) and B800 (pink) in the two structures are labeled and indicated with dashed lines. **(C)** Spectral analysis of the RC-LH complex. Fluorescence emissions are shown for nRC-LH (black) and dRC-LH (orange) complexes isolated from *Roseiflexus castenholzii* after excitation at 470 nm. **(D)** Fluorescence

excitation and absorption (1−T) spectra are shown as dotted and solid lines, respectively, for nRC-LH (black) and dRC-LH (orange). The Car-to-BChl energy transfer efficiency (vertical dashed line) was calculated by normalizing the fluorescence excitation and absorption spectra at 880 nm to 1.0.

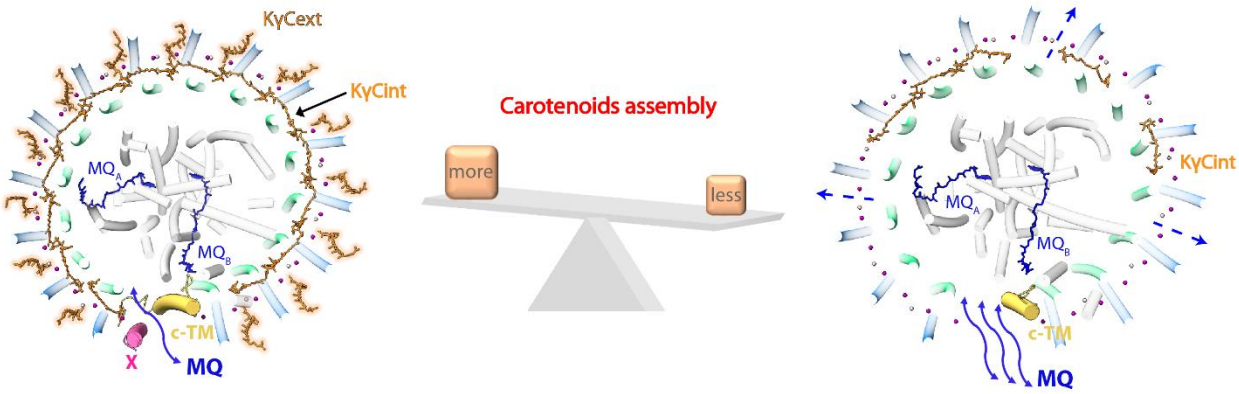

Figure 6. Schematic diagram of the carotenoid (Car) assembly related structural dynamics of *Roseiflexus castenholzii* RC-LH complex. In native RC-LH, incorporation of the external keto-γ-carotenes ($K\gamma C_{ext}$) and LH-bound B800s blocked the LHαβ interface. Alternatively, the subunit X disrupts the ring and forms a potential quinone channel with the c-TM, facilitating controlled quinone/quinol binding and shuttling. In dRC-LH, less carotenoid (Car) assembly exposed the LHαβ interface, absence of the subunit X and cytoplasmic region of c-TM concomitantly broadened the LH opening, which together accelerated the quinone/quinol exchange.

Table 1. Peptide mass fingerprinting (PMF) analysis of the *Roseiflexus castenholzii* nRC-LH that are separated by blue-native PAGE.

Subunit	Accession	Description	Score	Coverage
cyt *c*	BAC76415.1	cytochrome subunit of photosynthetic reaction center [*Roseiflexus castenholzii*]	131.79	40.94%
L and M	BAC76414.1	precursor for L and M subunits of photosynthetic reaction center [*Roseiflexus castenholzii*]	195.79	28.39%
LHα subunit	BAC76413.1	alpha subunit of light-harvesting 1 [*Roseiflexus castenholzii*]	97.78	100%
LHβ subunit	BAC76412.1	beta subunit of light-harvesting 1 [*Roseiflexus castenholzii*]	49.11	100%
Z subunit	WP_041331144.1	hypothetical protein [*Roseiflexus castenholzii*]		19.05%

Table 2. Cryo-EM data collection, refinement and validation statistics (to be continued).

	Native RC-LH at 10,000 lux (nRC-LH) (EMD-34838) (PDB 8HJU)	Carotenoid depleted RC-LH at 10,000 lux (dRC-LH) (EMD-34839) (PDB 8HJV)
Data collection and processing		
Magnification	64,000	81,000
Voltage (kV)	300	300
Electron exposure (e–/Å^2)	50	49.65
Defocus range (μm)	-1.0 to -2.3	-1.1 to -1.7
Pixel size (Å)	1.08	0.893
Symmetry imposed	C1	C1
Initial particle images (no.)	1,625,156	1,081,719
Final particle images (no.)	372,029	84,352
Map resolution (Å)	2.8	3.1
FSC threshold	0.143	0.143
Refinement		
Initial model used (PDB code)	5YQ7	Native RC-LH
Model resolution (Å)	2.8	3.1
FSC threshold	0.5	0.5
Map sharpening *B* factor (Å^2)	-98	-120
Model composition		
Non-hydrogen atoms	23,917	22,193
Protein residues	2,330	2,265
Ligands	97	67
B factors (Å^2)		
Protein	30.58	52.46
Ligand	30.11	55.37
R.m.s. deviations		
Bond lengths (Å)	0.011	0.010
Bond angles (°)	1.248	1.205
Validation		
MolProbity score	2.03	2.17
Clashscore	20.09	18.87
Poor rotamers (%)	0.76	0.84
Ramachandran plot		
Favored (%)	96.23	94.16
Allowed (%)	3.73	5.75
Disallowed (%)	0.04	0.09

	Native RC-LH at 100 lux (EMD-35988) (PDB 8J5O)	Native RC-LH at 2,000 lux (EMD-35989) (PDB 8J5P)
Data collection and processing		
Magnification	81,000	81,000
Voltage (kV)	300	300
Electron exposure (e–/Å^2)	50	50
Defocus range (μm)	-1.2 to -2.0	-1.2 to -2.0
Pixel size (Å)	0.893	0.893
Symmetry imposed	C1	C1
Initial particle images (no.)		
Final particle images (no.)		
Map resolution (Å)	2.9	3.1
FSC threshold	0.143	0.143
Refinement		
Initial model used (PDB code)	Native RC-LH	Native RC-LH
Model resolution (Å)	2.8	3.1
FSC threshold	0.5	0.5
Map sharpening *B* factor (Å^2)	-98	-120
Model composition		
Non-hydrogen atoms	23,691	23,737
Protein residues	2,318	2,331
Ligands	93	92
B factors (Å^2)		
Protein	27.54	39.01
Ligand	24.73	37.37
R.m.s. deviations		
Bond lengths (Å)	0.018	0.017
Bond angles (°)	1.915	1.850
Validation		
MolProbity score	1.97	1.98
Clashscore	18.79	17.69
Poor rotamers (%)	0.00	0.30
Ramachandran plot		
Favored (%)	96.79	96.50
Allowed (%)	3.21	3.46
Disallowed (%)	0.00	0.04

Table 3. Edge-to-edge distance (Å) of KγC$_{int}$ to LH-bound B800/B880s in the nRC-LH and dRC-LH complexes from *Roseiflexus castenholzii*.

nRC-LH	**1**	**2**	**3**	**4**	**5**	**6**	**7**	**8**	**9**	**10**	**11**	**12**	**13**	**14**	**15**
B800	—	3.6	4.2	3.7	3.6	4.1	3.5	3.4	3.7	3.9	4.0	3.8	4.2	3.7	—
B880	—	4.3	3.8	3.8	3.9	3.9	4.2	4.0	3.9	4.3	4.0	4.1	3.6	3.6	3.7
dRC-LH	**1**	**2**	**3**	**4**	**5**	**6**	**7**	**8**	**9**	**10**	**11**	**12**	**13**	**14**	**15**
B800	—	—	—	—	4.2	—	3.4	—	4.1	3.3	3.9	—	—	—	—
B880	—	—	—	—	4.0	—	4.2	—	4.4	3.8	4.0	—	—	—	—

Table 4. Edge-to-edge distance (Å) of KγC$_{ext}$ to LH-bound B800/B880s in the nRC-LH complex from *Roseiflexus castenholzii*.

nRC-LH	1	2	3	4	5	6	7	8	9	10	11	12	13	14	15
B800	—	3.7	3.4	3.9	3.8	3.8	3.7	3.3	3.5	3.2	3.3	3.4	3.5	3.5	4.2
B880	—	4.8	5.0	5.0	5.0	4.1	4.2	4.3	4.8	4.8	5.1	4.7	4.2	4.8	4.6

Table 5. Distances (Å) between the LHαβ transmembrane (TM) helices of the nRC-LH and dRC-LH complexes from *Roseiflexus castenholzii*.

The distance is measured between LHαβn and LHαβ (n+1).

* the distances from LHα15 Met-22 to C-TM Val-33, and LHβ15 Ile-39 to subunit X.

† the distances from LHα1 Val-29 to C-TM Tyr-44, and LHβ1 Leu-37 to subunit X.

nRC-LH	**1**	**2**	**3**	**4**	**5**	**6**	**7**	**8**	**9**	**10**	**11**	**12**	**13**	**14**	**15***	**16†**
LHα	14.8	14.7	14.6	14.3	14.4	14.7	15.4	14.9	15.4	14.6	14.7	15.0	14.5	14.4	19.4	9.7
LHβ	20.0	19.8	20.0	20.4	20.2	20.0	19.8	19.9	19.7	20.1	20.0	19.9	20.1	20.1	11.2	28.1
dRC-LH	**1**	**2**	**3**	**4**	**5**	**6**	**7**	**8**	**9**	**10**	**11**	**12**	**13**	**14**	**15***	**16†**
LHα	15.4	15.4	15.3	15.0	14.9	15.3	16.2	15.5	16.1	15.2	15.4	15.6	15.3	14.9	19.6	10.2
LHβ	21.0	20.7	20.9	21.2	20.9	21.0	20.5	20.9	20.6	20.8	21.0	20.7	20.9	20.9	—	—

Table 6. The distances (Å) between adjacent LH-bound B880s of the nRC-LH and dRC-LH complexes from *Roseiflexus castenholzii*.

*distance between the B880 bound by the same transmembrane pairs of LH.

†distance between the B880 bound by adjacent transmembrane pairs of LH.

nRC-LH	**1**	**2**	**3**	**4**	**5**	**6**	**7**	**8**	**9**	**10**	**11**	**12**	**13**	**14**	**15**
Edge-to-edge*	3.3	3.1	3.4	3.4	3.6	3.8	3.7	3.8	3.7	3.6	3.5	3.6	3.5	3.6	3.8
Edge-to-edge†	3.5	3.4	3.6	3.6	3.4	4.0	3.6	3.8	3.5	3.5	3.3	3.7	3.6	3.6	19.1
Mg-to-Mg*	10.2	9.9	9.8	9.9	9.7	9.8	9.9	10.0	9.9	9.9	9.8	9.6	9.7	9.3	9.8
Mg-to-Mg†	7.6	7.5	7.7	7.7	7.6	7.6	7.6	7.5	7.6	7.8	7.7	7.9	7.9	7.9	26.2
dRC-LH	**1**	**2**	**3**	**4**	**5**	**6**	**7**	**8**	**9**	**10**	**11**	**12**	**13**	**14**	**15**
Edge-to-edge*	3.5	3.5	3.5	3.7	3.5	3.7	3.7	3.8	3.9	3.8	3.6	3.5	3.6	3.3	3.7
Edge-to-edge†	4.1	3.8	4.0	3.8	3.9	3.8	4.1	4.0	4.1	3.9	3.9	3.9	3.9	3.8	20.2
Mg-to-Mg*	9.7	9.7	9.5	9.6	9.6	9.6	9.4	9.7	9.7	9.6	9.5	9.4	9.5	9.3	9.2
Mg-to-Mg†	9.0	8.7	8.8	8.8	8.4	8.9	8.8	8.6	8.8	8.8	8.9	9.0	9.0	8.7	27.2

Table 7. The distances (Å) between LH-bound B800s of the nRC-LH and dRC-LH complexes from *Roseiflexus castenholzii*.

nRC-LH	**1**	**2**	**3**	**4**	**5**	**6**	**7**	**8**	**9**	**10**	**11**	**12**	**13**	**14**	**15**
Edge-to-edge	15.4	15.5	15.5	15.4	15.4	15.6	15.6	15.4	15.6	15.5	15.5	15.6	15.6	15.2	33.4
Mg-to-Mg	18.4	18.3	18.4	18.5	18.5	18.5	18.5	18.3	18.4	18.4	18.5	18.5	18.4	18.3	38.5
dRC-LH	**1**	**2**	**3**	**4**	**5**	**6**	**7**	**8**	**9**	**10**	**11**	**12**	**13**	**14**	**15**
Edge-to-edge	15.8	15.9	16.0	15.7	15.8	16.2	15.9	15.8	16.1	15.8	16.0	16.1	15.8	15.8	33.2
Mg-to-Mg	19.1	19.1	19.3	19.1	19.2	19.4	19.1	19.2	19.2	19.1	19.3	19.3	19.1	19.2	38.3

Table 8. The Mg-to-Mg distances between LH-bound B880s and the nearest special pair of BChls in the RC of *Roseiflexus castenholzii* nRC-LH and dRC-LH complexes.

* the distances from Mg^{2+} of the first LH-bound B880 to the nearest special pair of BChls.

† the distances from Mg^{2+} of the second LH-bound B880 to the nearest special pair of BChls.

nRC-LH	**1**	**2**	**3**	**4**	**5**	**6**	**7**	**8**	**9**	**10**	**11**	**12**	**13**	**14**	**15**
Mg-to-Mg*	40.3	42.4	44.7	47.2	46.8	43.9	40.2	37.3	36.5	37.7	40.6	43.7	44.5	44.8	44.2
Mg-to-Mg†	41.5	43.8	46.3	48.1	45.6	42.0	38.5	36.8	36.8	39.6	42.6	44.5	44.9	44.8	43.6
dRC-LH	**1**	**2**	**3**	**4**	**5**	**6**	**7**	**8**	**9**	**10**	**11**	**12**	**13**	**14**	**15**
Mg-to-Mg*	42.0	44.8	47.2	49.9	49.0	45.8	42.0	39.1	38.3	39.7	43.0	46.0	46.2	46.4	45.4
Mg-to-Mg†	43.1	45.8	48.5	50.0	47.2	43.8	40.2	38.4	38.6	41.3	44.5	46.0	46.3	46.1	44.6

Table 9. Apparent Michaelis constants of menaquinone-4 as electron acceptor in the auracyanin (Ac) oxidation assay, in presence of the *Roseiflexus castenholzii* nRC-LH or dRC-LH complex.

	nRC-LH	**dRC-LH**
K_m (μM)	32.24 ±6.84	10.43 ±1.23
k_{cat} (min^{-1})	82.61 ±9.09	63.83 ±2.49
k_{cat}/K_m	2.56 ±0.49	6.12 ±0.62

Movie 1. Top-view of the conformational changes between native RC-LH (nRC-LH) and carotenoid depleted RC-LH (dRC-LH) complexes from *Roseiflexus castenholzii*. The color scheme is same as Fig. 1 and 4.

Movie 2. Conformational changes of the LH ring opening between native RC-LH (nRC-LH) and carotenoid depleted RC-LH (dRC-LH) complexes from *Roseiflexus castenholzii*. The color scheme is same as Fig. 4C.

Figure supplements for

Carotenoid assembly regulates quinone diffusion and the *Roseiflexus castenholzii* reaction center-light harvesting complex architecture

Jiyu Xin, Yang Shi and Xin Zhang *et al*.

*Corresponding author. Email: xuxl@hznu.edu.cn

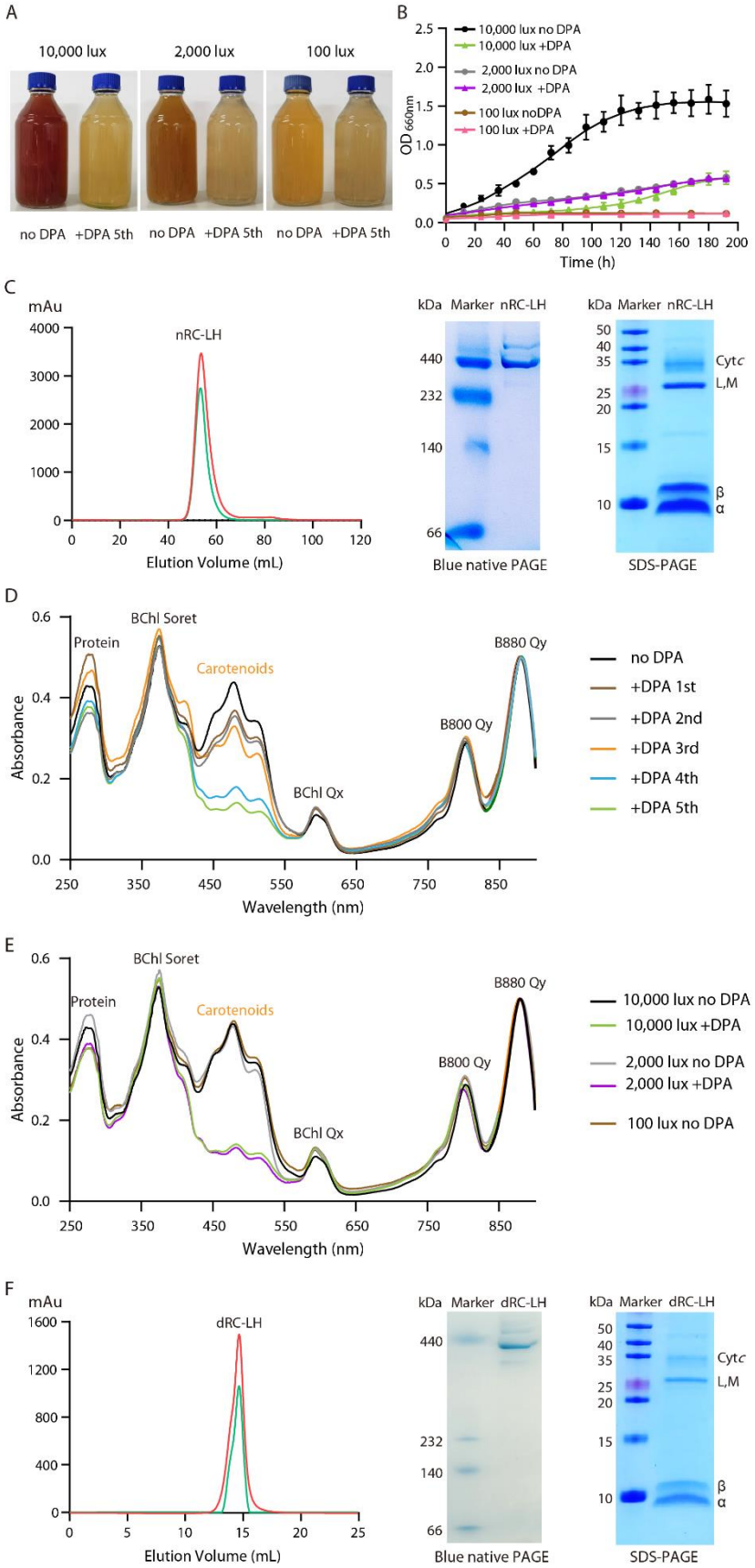

Figure 1—figure supplement 1. Purification and verification of the native (nRC-LH) and carotenoid depleted RC-LH (dRC-LH) complexes from *Roseiflexus castenholzii*. (A)

Appearance of the native *R. castenholzii* (left) and the fifth subculture of diphenylamine (DPA)-treated (right) cells, which were cultured anaerobically under 10,000 lux, 2,000 lux and 100 lux light intensities, respectively. **(B)** Growth curves of the native *R. castenholzii* and the fifth subculture of diphenylamine (DPA)-treated cells grown under 10,000 lux, 2,000 lux and 100 lux light intensities. Data are shown as the mean ± standard deviations (n=3). **(C)** Representative gel-filtration chromatography, blue native PAGE and SDS-PAGE of the nRC-LH complex from *R. castenholzii* cultured under 10,000 lux. The chromatography diagram of absorption at 280 nm (red) and 800 nm (green) of nRC-LH is shown. The subunits L, M and cyt *c* subunits of RC and the αβ apoproteins of the LH are labeled. **(D)** Absorption spectrum analyses of RC-LH complexes purified from *R. castenholzii* grown under 10, 000 lux light intensity. Black corresponds to untreated cells; brown, gray, orange, blue and green correspond to carotenoid (Car)-depleted cells from five consecutive subcultures of DPA-treated cells, respectively. The characteristic Qy bands of B800 and B880, the Qx and Soret bands of bacteriochlorophylls (BChls), and the absorption peaks of Cars are labeled. **(E)** Absorption spectrum analyses of RC-LH complexes purified from *R. castenholzii* cells with or without DPA treatment under light intensities of 10,000 lux, 2,000 lux, and 100 lux. **(F)** Representative gel-filtration chromatography, blue native PAGE and SDS-PAGE of the dRC-LH complex purified from *R. castenholzii* cultured under 10,000 lux.

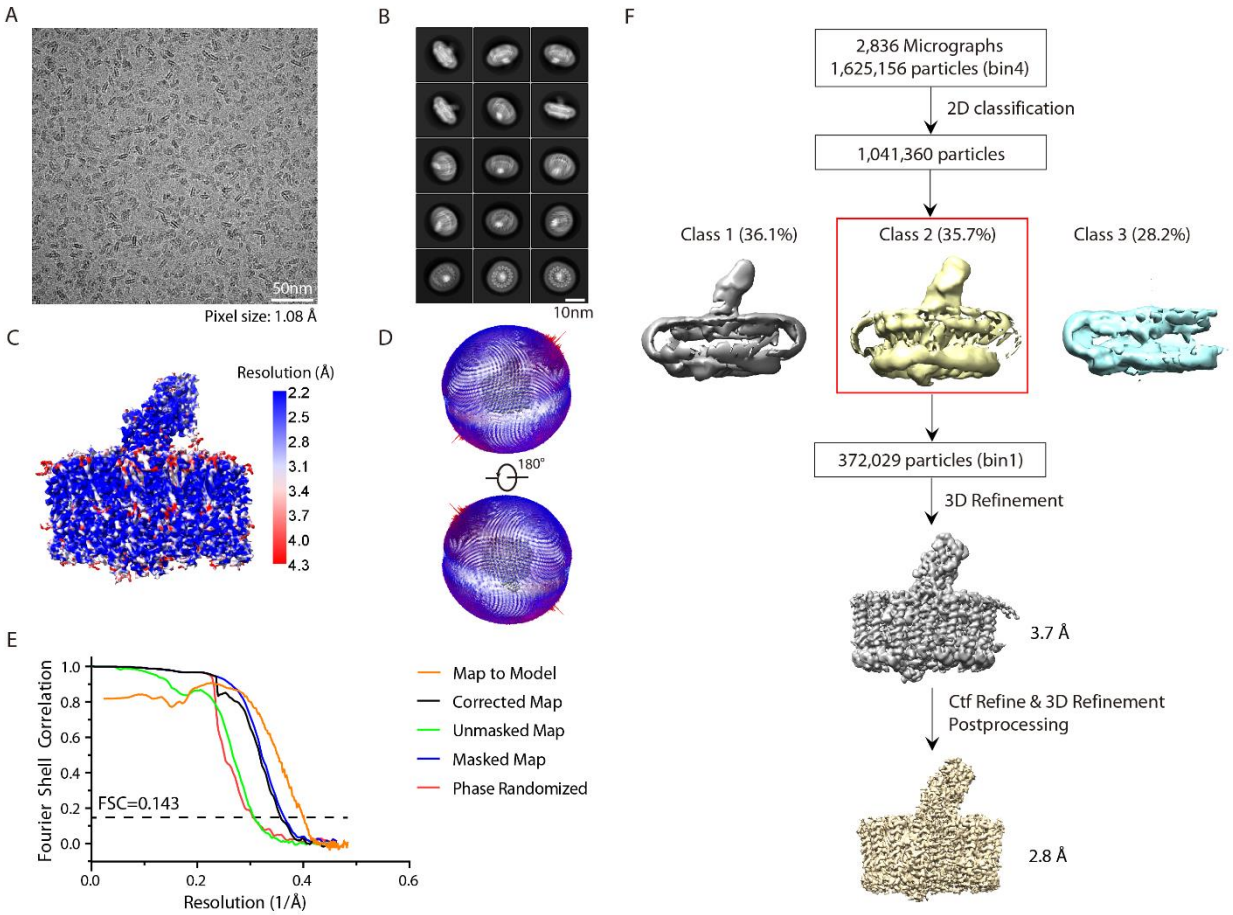

Figure 1—figure supplement 2. Cryo-EM analyses of the native RC-LH (nRC-LH) complex from *Roseiflexus castenholzii*. (A) A representative raw cryo-EM micrograph of the nRC-LH complex purified from the cells grown under 10,000 lux. **(B)** Representative reference-free 2D class averages of the nRC-LH complex. **(C)** Local resolution of the cryo-EM map estimated by ResMap. **(D)** The different views of angular distribution of the nRC-LH complex particles in final reconstruction. The direction and length of each cylinder represent the direction and amount of particles. **(E)** The gold-standard Fourier shell correlation (FSC) curve of the cryo-EM map (Corrected map, black; Unmasked, green; Masked, blue; Phase randomized, red) and the FSC curve between the map and the final refined model (orange). **(F)** Cryo-EM data processing workflow for the native RC-LH (nRC-LH) complex. All structural figures here are generated with ChimeraX.

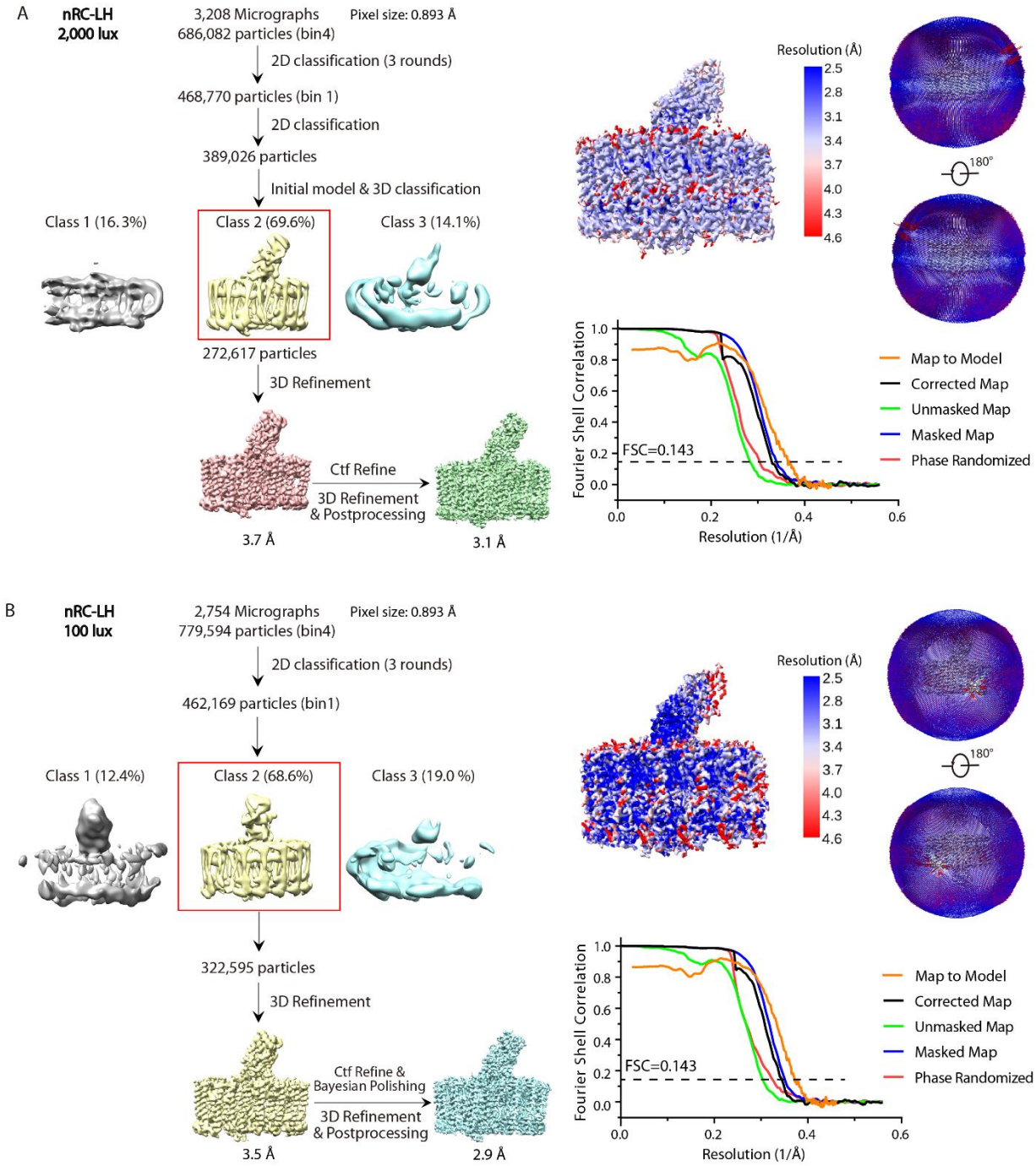

Figure 1—figure supplement 3. Cryo-EM analysis of the native RC-LH complexes purified from *Roseiflexus castenholzii* grown under 2,000 lux or 100 lux light intensities. (A, B) Cryo-EM data processing workflow for the native RC-LH purified from *R. castenholzii* grown under 2,000 lux (A) and 100 lux (B) light intensities. The local resolution of the cryo-EM map and the angular distribution of particles in final reconstruction are shown in upper right panel.

The gold-standard Fourier shell correlation (FSC) curve of the cryo-EM map and the FSC curve between the map and the final refined model are shown in lower right panel.

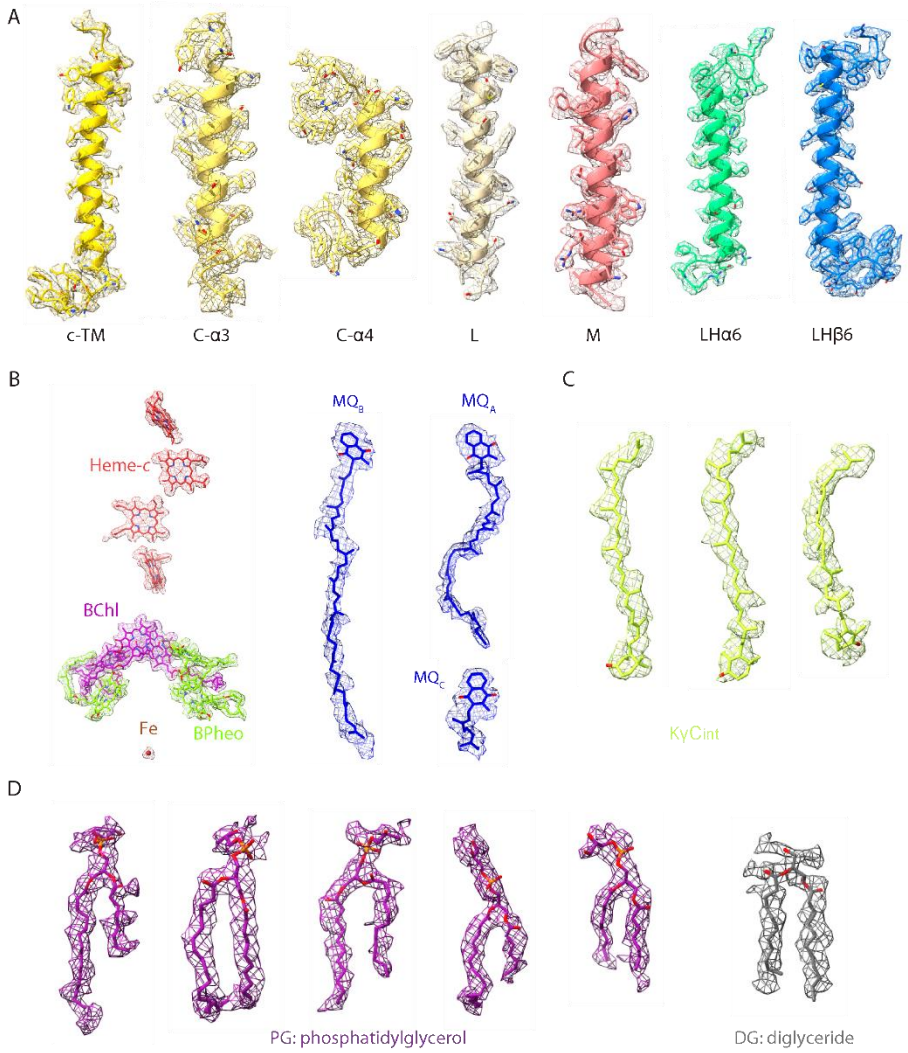

Figure 1—figure supplement 4. Cryo-EM densities and structural models of the RC-LH complex from *Roseiflexus castenholzii*. (A) EM density maps of representative α-helices in the native RC-LH (nRC-LH) complex are shown in mesh forms. The corresponding atomic models are shown in stick forms. **(B)** The cofactors in the native RC were docked into the EM density map. **(C)** A density map of the keto-γ-carotenes ($K\gamma C_{int}$) bound in LH ring interior of the carotenoid depleted dRC-LH complex. The corresponding atomic models are colored in limon. **(D)** EM map densities fitted with resolved lipids for the nRC-LH.

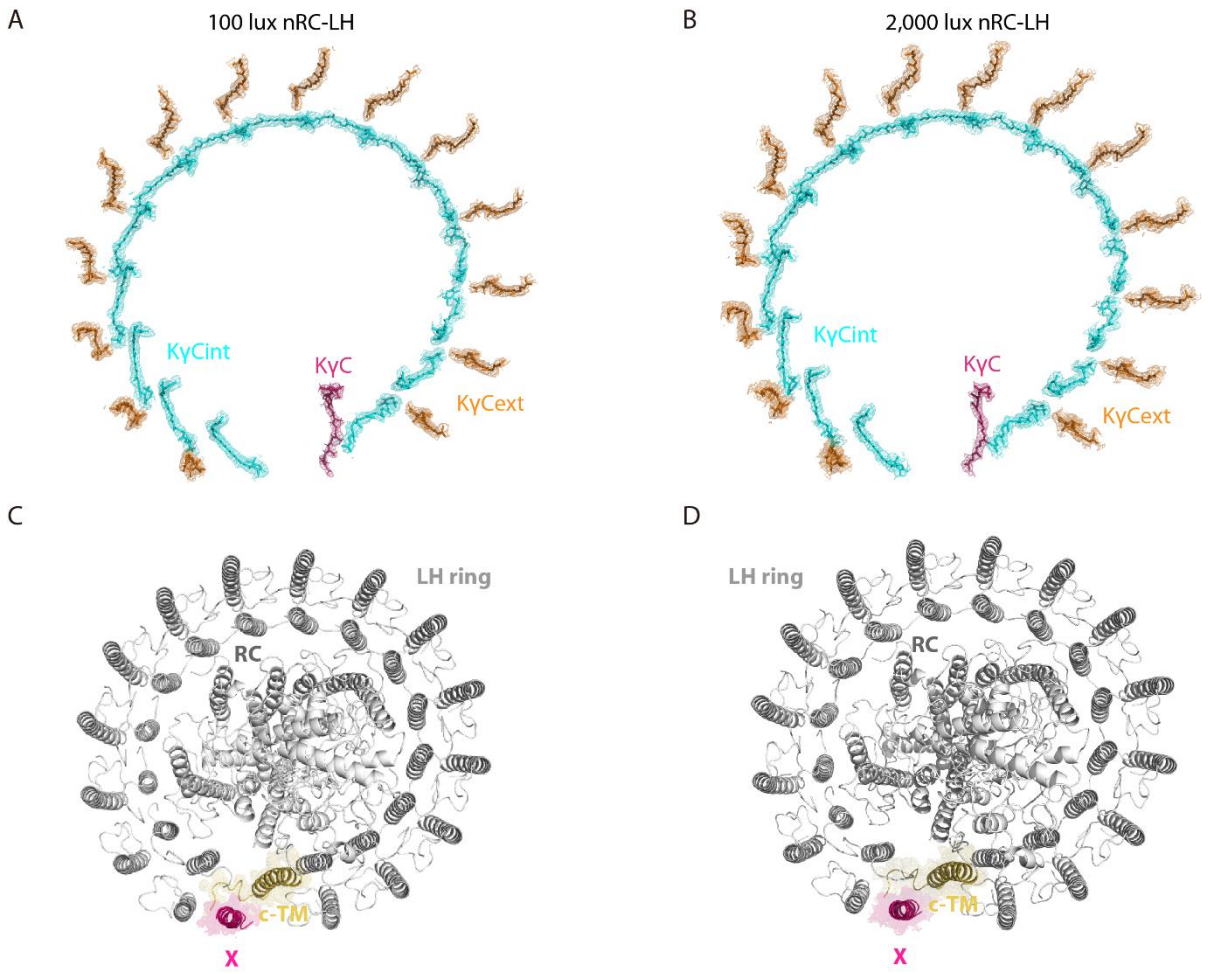

Figure 1—figure supplement 5. The structures of native RC-LH (nRC-LH) complexes obtained from *Roseiflexus castenholzii* grown under 2,000 lux and 100 lux light intensities. **(A, B)** The structural models of the interior keto-γ-carotenes ($K\gamma C_{int}$), exterior keto-γ-carotenes ($K\gamma C_{ext}$), and a KγC at the LH ring opening in the nRC-LH complexes obtained at 100 lux (A) and 2,000 lux (B) were fitted in the EM density map. **(C, D)** The structural models of proteins in the nRC-LH complexes obtained at 100 lux (C) and 2,000 lux (D). The corresponding EM densities of subunit X and c-TM are shown in surface forms.

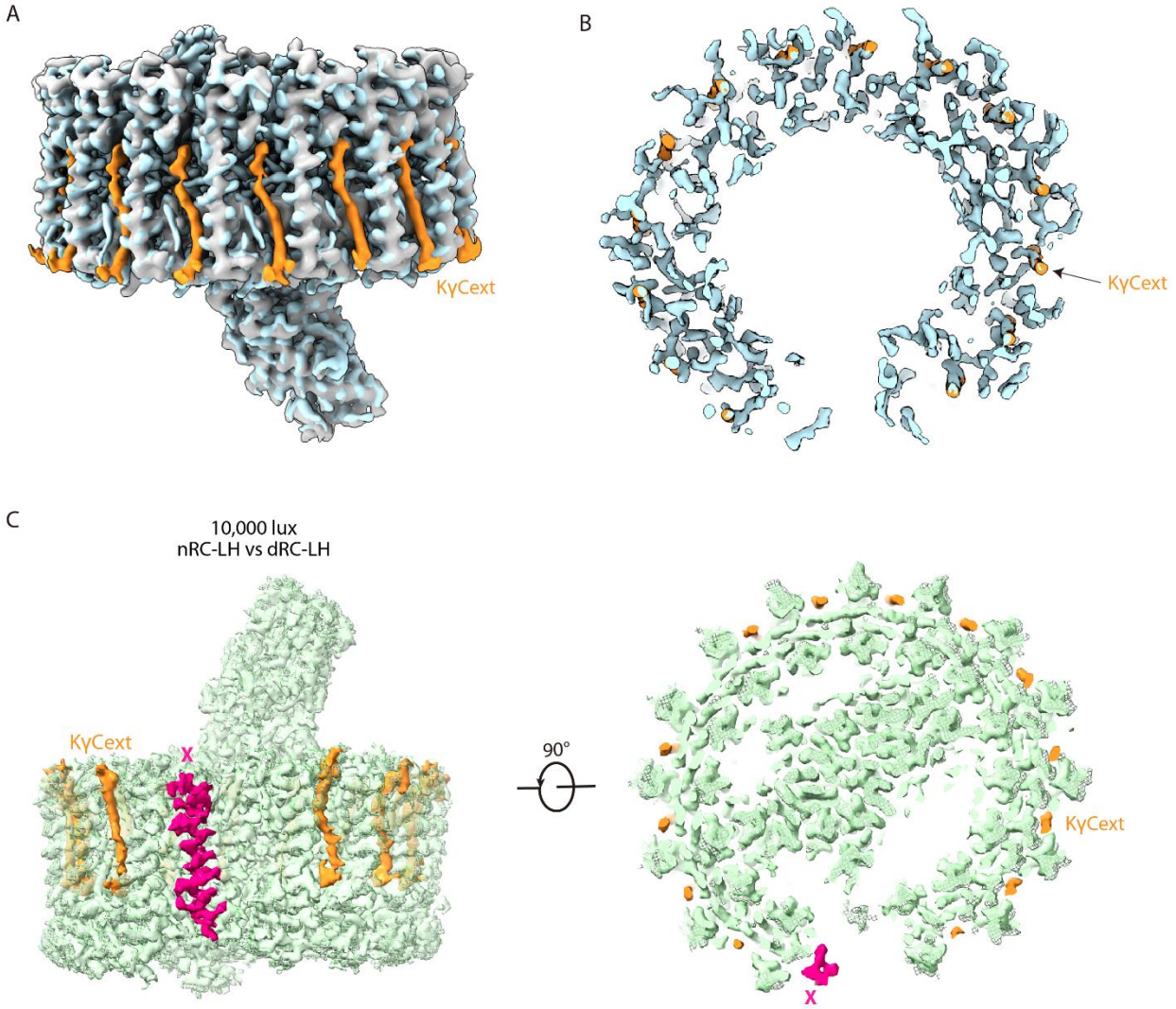

Figure 1—figure supplement 6. Comparison of the cryo-EM maps of the nRC-LH and dRC-LH complexes obtained at 2,000 lux and 10,000 lux light intensities. (A) Superposition of cryo-EM maps of the reported 4.1-Å RC-LH model and the low-pass filtered nRC-LH map that was obtained at the same 2,000 lux light intensities. The cryo-EM map of nRC-LH complex (blue) was low-pass filtered to the same 4.1-Å resolution as the reported RC-LH (gary). The cryo-EM densities for the exterior keto-γ-carotenes ($K\gamma C_{ext}$) were highlighted in orange. **(B)** The global density differences between the reported 4.1-Å RC-LH model and the nRC-LH complex obtained at 2,000 lux. The difference map of $K\gamma C_{ext}$ is shown in orange. **(C)** Superposition of cryo-EM maps of the nRC-LH (surface) and dRC-LH (mesh) complexes obtained at 10,000 lux.

The cryo-EM densities of subunit X and keto-γ-carotenes ($K\gamma C_{ext}$) were highlighted in hot pink and orange, respectively. All structural figures here are generated with ChimeraX.

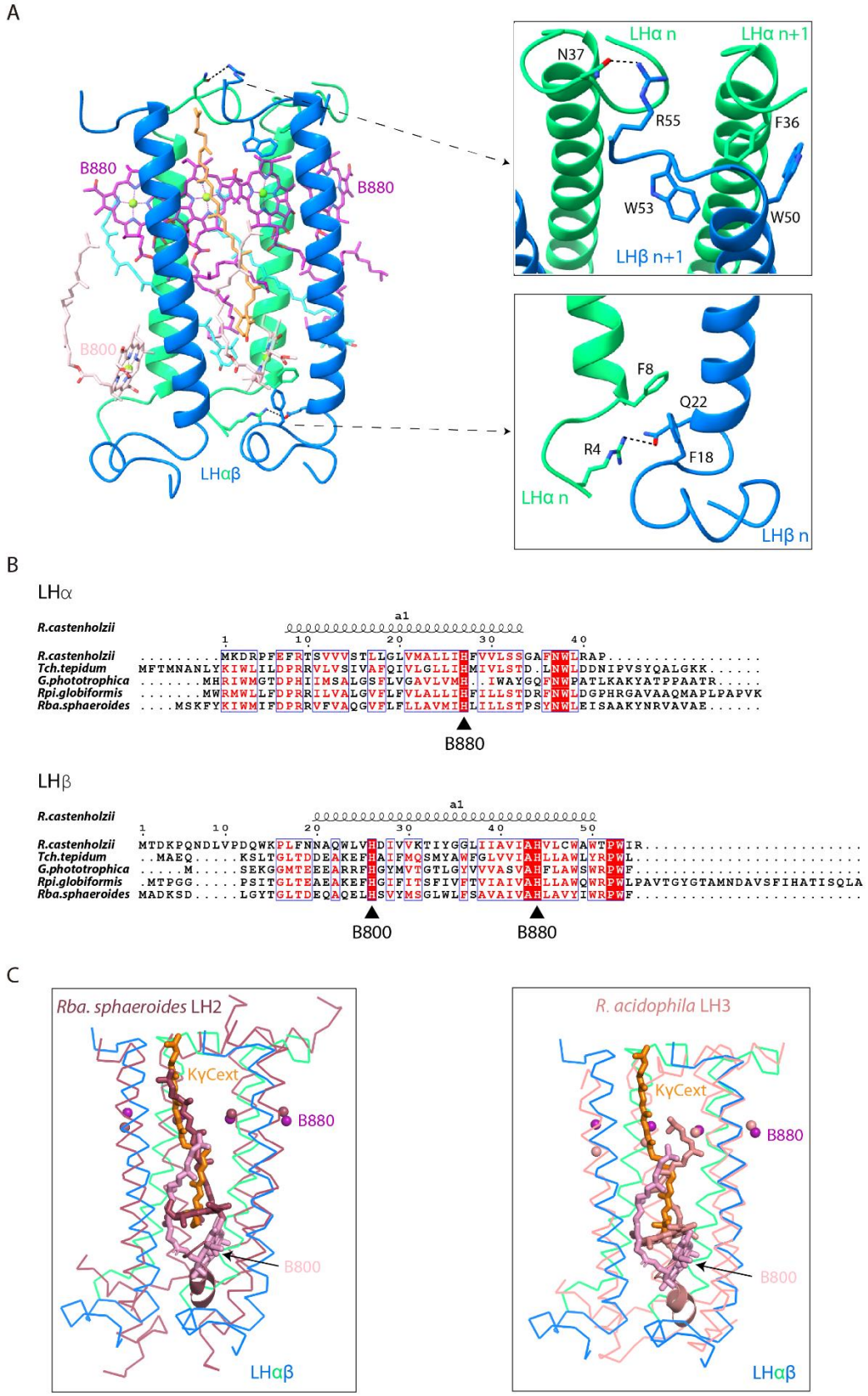

Figure 2—figure supplement 1. Interactions between LHαβ heterodimers in the native RC-LH (nRC-LH) complex from *Roseiflexus castenholzii*. (A) The left panel shows the

interactions between LHα and LHβ polypeptides. Close-up views of interactions between the C-terminus (top) or N-terminus (bottom) of LHα and LHβ are shown on the right. Interacting amino acid residues are shown in stick forms. **(B)** Structure based sequence alignment of the LHα and LHβ subunits from *Roseiflexus* (*R.*) *castenholzii* and the representative purple bacteria. *Thermochromatium (Tch.) tepidum* (PDB ID: 5Y5S), *Gemmatimonas* (*G.*) *phototrophica* (PDB ID: 7O0U), *Rhodopila* (*Rpi.*) *globiformis* (PDB ID: 7XXF) and *Rhodobacter* (*Rba.*) *sphaeroides* (PDB ID: 7F0L). **(C)** Structural comparison of LHαβ heterodimers from *R. castenholzii* nRC-LH with *Rba. sphaeroides* LH2 (left, PDB ID: 7PBW) and *Rhodopseudomonas* (*R.*) *acidophila* LH3 (right, PDB ID: 1IJD) that both bind B800s. The LH-bound B800 and exterior keto-γ-carotenes ($K\gamma C_{ext}$) in nRC-LH are shown as pink and orange sticks, respectively. The B800 bound in *Rba. sphaeroides* LH2 (violet-purple) and *R. acidophila* LH3 (salmon) are also shown in stick forms. Mg atoms of LH-bound B880 are shown in spheres.

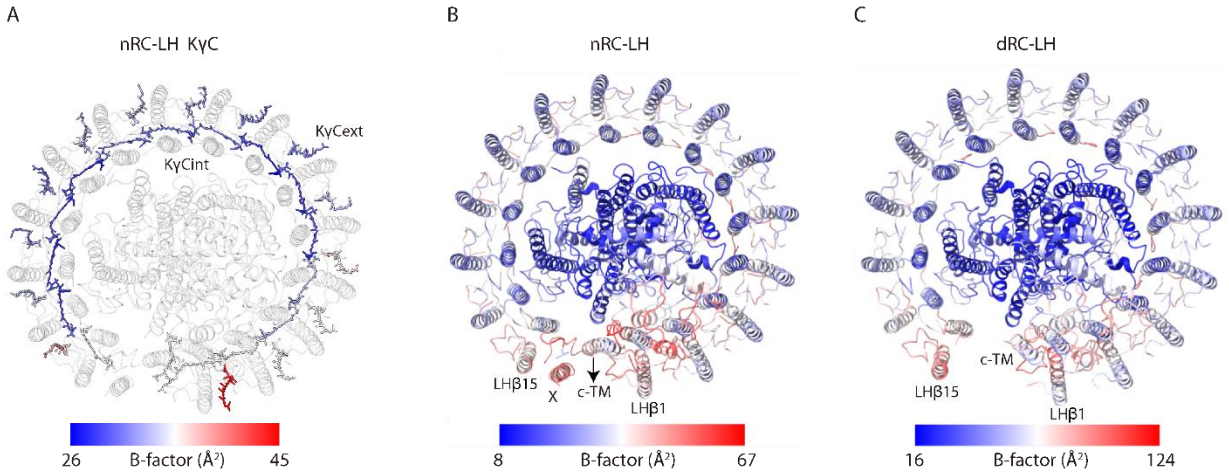

Figure 2—figure supplement 2. B-factors distribution of the nRC-LH and dRC-LH complexes from *Roseiflexus castenholzii.* (A) B-factors distribution of the keto-γ-carotenes in nRC-LH. B-factor values are indicated by color. Protein subunits of the nRC-LH are shown in gray. **(B)** B-factors distribution of protein subunits in the nRC-LH complex. **(C)** B-factor distribution of protein subunits in the dRC-LH complex. B-factor values are indicated by color. The subunit X, c-TM of cyt *c* subunit, LHβ1 and LHβ15 with higher B-factor are indicated.

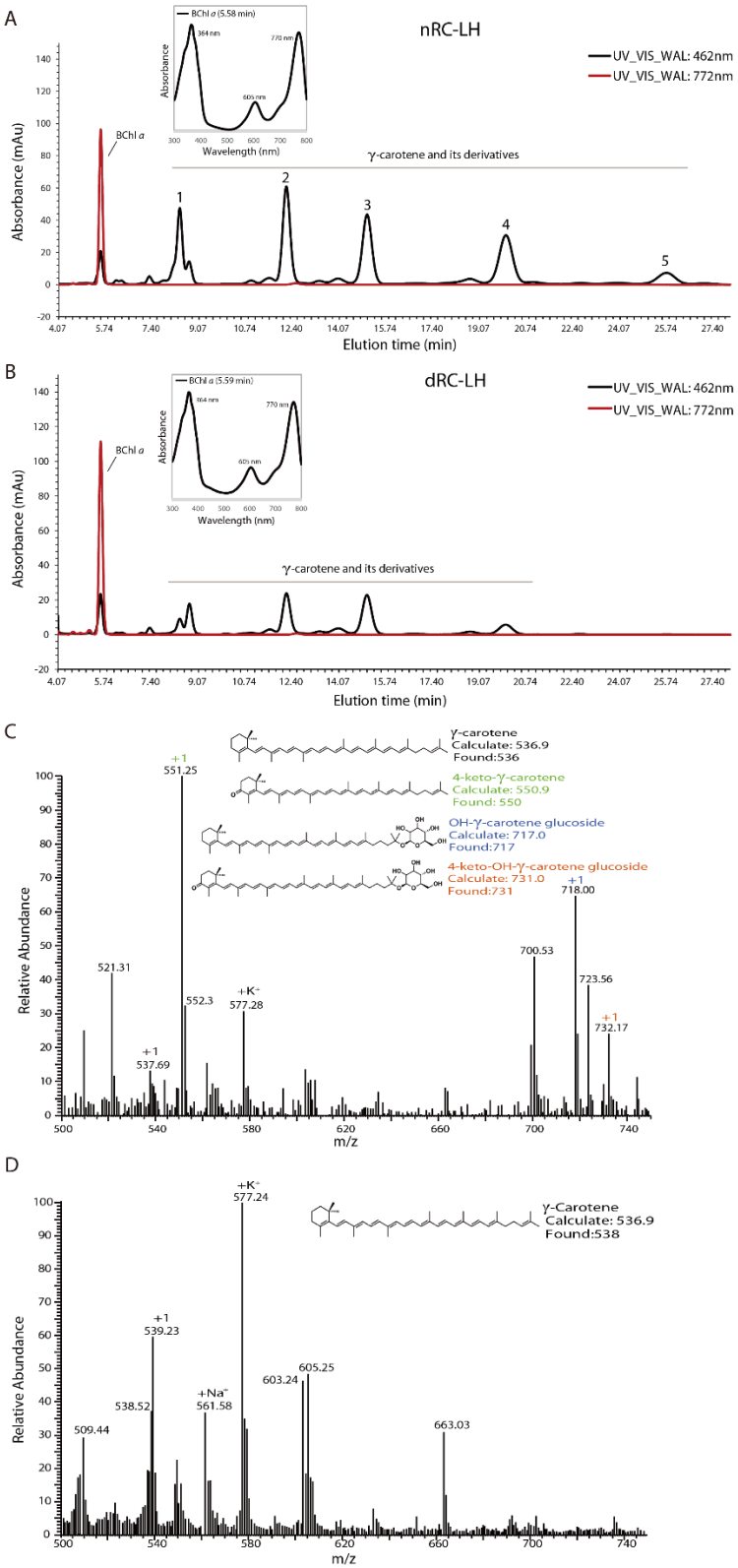

Figure 2—figure supplement 3. High performance liquid chromatography (HPLC)-Mass spectrometry (MS) analyses of the pigments in RC-LH complex from *Roseiflexus castenholzii*. (A, B) HPLC analysis of the extracted pigments of nRC-LH (A) and dRC-LH (B) that were isolated from the fifth sub-culture of DPA-treated *R. castenholzii* cells. The pigments

were detected by their absorbance at 462 nm (black line) and 772 nm (red line), based on the characteristic absorption spectrum and LC-MS. The first peak at retention time of 5.58 min was identified to be the bacteriochlorophylls *a* (BChl), which was characterized with absorption peaks at 364nm, 605 nm and 770 nm. The following peaks 1-5 were all characterized to be γ-carotene and its derivatives. **(C, D)** MS analysis of the HPLC peak 1 (C) and peaks 2-5 (D) using atmospheric pressure chemical ionization (APCI) method. The calculated and found molecular weights of γ-carotene, 4-keto-γ-carotene, OH-γ-carotene glucoside and 4-keto-OH-γ-carotene glucoside were both ~536 Da, ~550 Da, ~717 Da and ~731 Da, respectively. Both the measured m/z values and the chemical formula of γ-carotene and its derivatives were indicated. All the experiments were repeated three times.

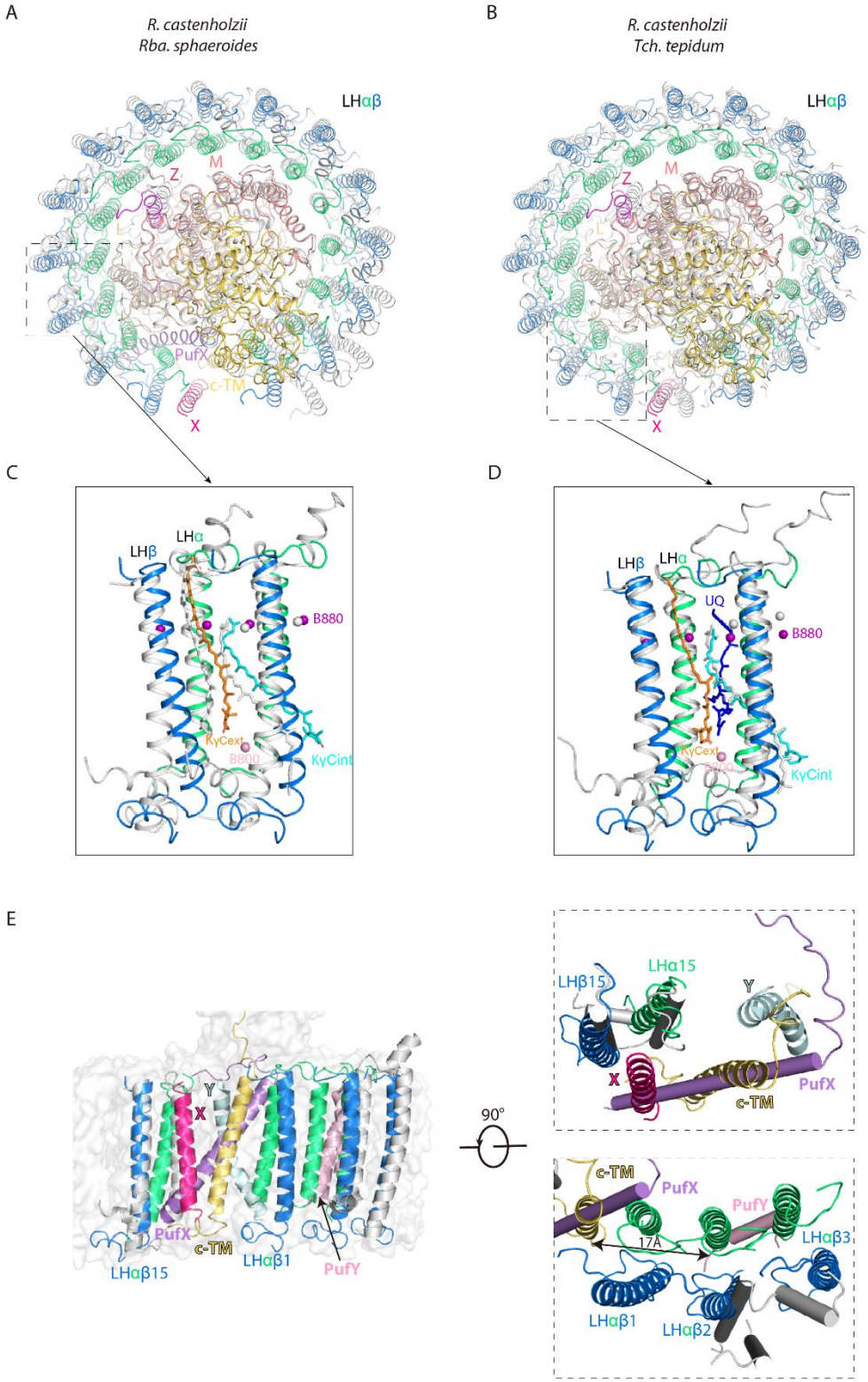

Figure 2—figure supplement 4. Structural comparison of the native RC-LH (nRC-LH) from *Roseiflexus (R.) castenholzii* with the RC-LH1s from *Rhodobacter* (*Rba.*) *sphaeroides* and *Thermochromatium* (*Tch.*) *tepidum*. (A, B) Overall structural comparison of *R. castenholzii* nRC-LH (colored) with *Rba. sphaeroides* RC-LH1 (white, PDB ID: 7F0L) and *Tch.*

tepidum RC-LH1 (white, PDB ID: 5Y5S). **(C, D)** Superposition of LHαβ heterodimers from *R. castenholzii* nRC-LH with *Rba. sphaeroides* RC-LH1 (C) and *Tch.tepidum* RC-LH1 (D). *R. castenholzii* nRC-LH is shown in cartoon form, except for the Mg atoms of LH-bound BChls (B800/B880) are shown in spheres. Interior keto-γ-carotenes ($K\gamma C_{int}$) and exterior keto-γ-carotenes ($K\gamma C_{ext}$) in the nRC-LH are shown as cyan and orange sticks, respectively. The carotenoids in *Rba. sphaeroides* and *Tch. tepidum* RC-LH1 are shown as white sticks. The ubiquinone (UQ) bound in *Tch. tepidum* LHαβ is colored blue. **(E)** Superposition of *R. castenholzii* nRC-LH with *Rba. sphaeroides* RC-LH1 at the LHαβ15 heterodimer to show the spatial organizations of subunit X, c-TM and Y with that of PufX and PufY (or protein -U). The right panel shows top view of the superposed region near PufY. Arrow shows the distance (~17 Å) between the N-terminus of the transmembrane helices of c-TM and PufY. The model of *R. castenholzii* nRC-LH is colored same as Fig. 1. The model of *Rba. sphaeroides* RC-LH1 is colored in white, with PufX colored in arsenic and PufY colored in light pink.

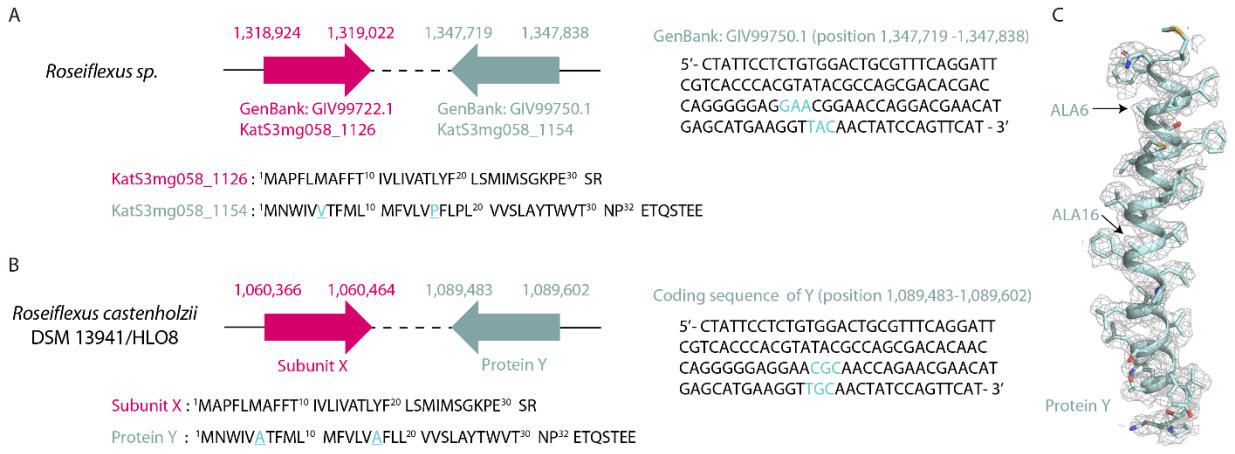

Figure 2—figure supplement 5. Assignment the amino acid sequences and coding sequences of subunit X and protein Y in *Roseiflexus sp.* and *Roseiflexus castenholzii* DSM 13941/HLO8. (A) Amino acid sequences of the KatS3mg058_1126 and KatS3mg058_1154 proteins, and the coding sequence of KatS3mg058_1154 in *Roseiflexus sp*. genome. **(B)** Amino acid sequences of subunit X and protein Y, and the coding sequence of protein Y in the genome of *Roseiflexus castenholzii* DSM 13941/HLO8 strain. The non-conserved amino acid residues in protein Y and KatS3mg058_1154 are colored in blue and underlined. **(C)** The structural model of protein Y in the native RC-LH were docked into the EM density map. Arrows indicate the non-conserved amino acid residues of protein Y compared with *Roseiflexus sp* KatS3mg058_1154.

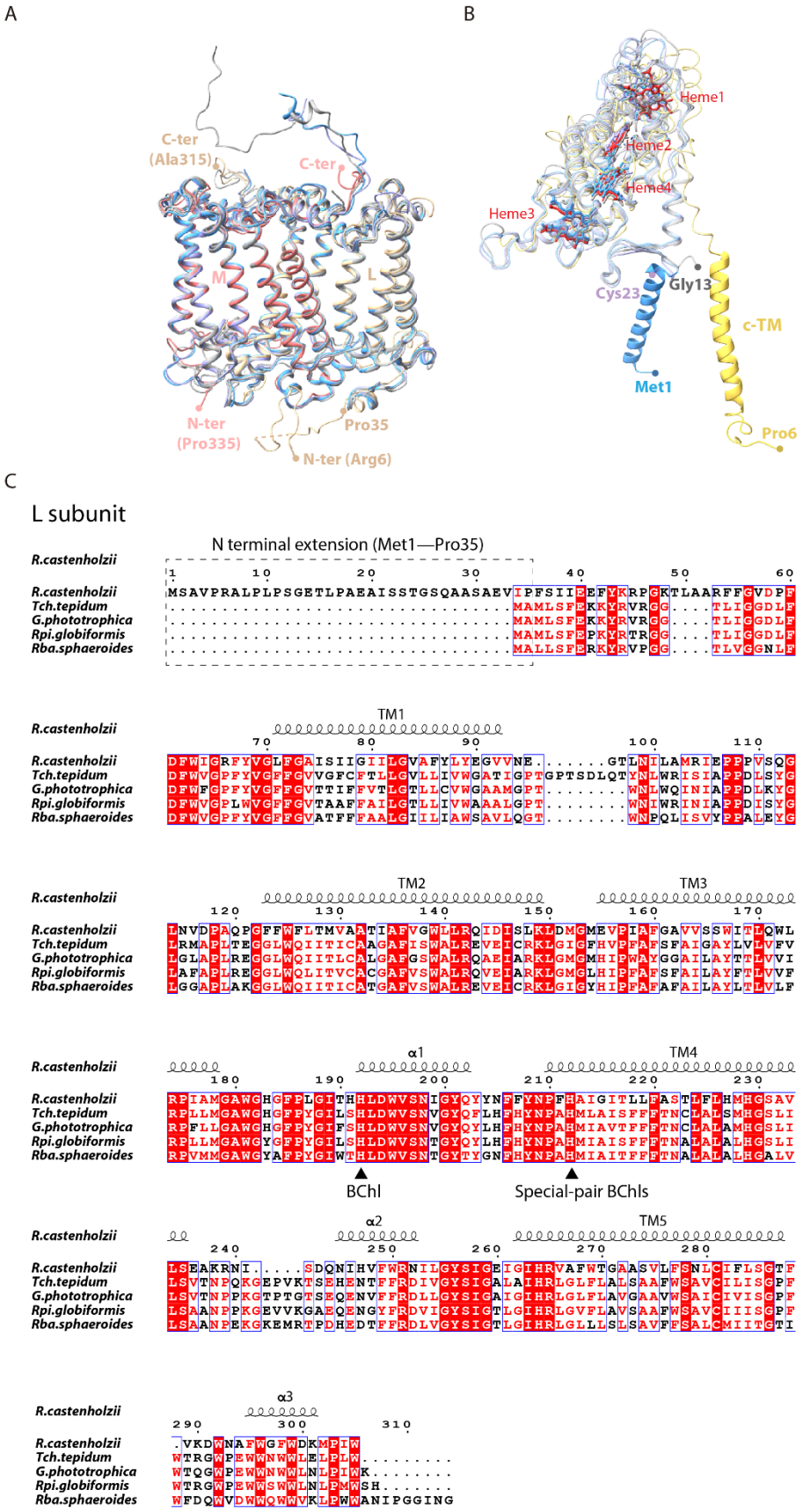
A
B
C-ter
(Ala315)
C-ter
M
L
N-ter
(Pro335)
Pro35
N-ter (Arg6)
Heme1
Heme2
Heme4
Heme3
Cys23
Gly13
c-TM
Met1
Pro6
C
L subunit
N terminal extension (Met1—Pro35)
R.castenholzii
Tch.tepidum
G.phototrophica
Rpi.globiformis
Rba.sphaeroides
TM1
TM2
TM3
α1
TM4
BChl
Special-pair BChls
α2
TM5
α3

M subunit

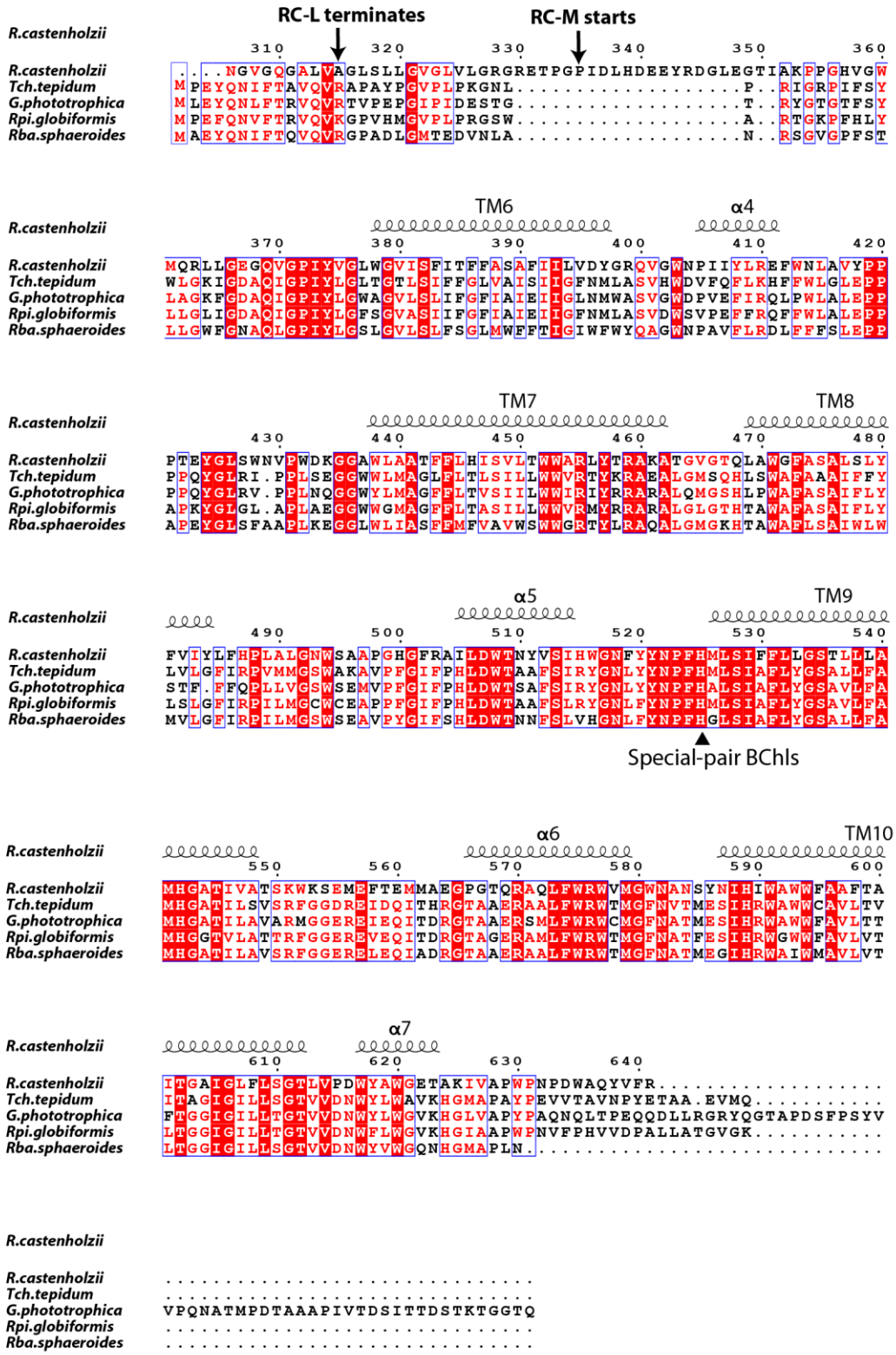
RC-L terminates
RC-M starts
R.castenholzii
Tch.tepidum
G.phototrophica
Rpi.globiformis
Rba.sphaeroides
TM6
α4
TM7
TM8
α5
TM9
Special-pair BChls
α6
TM10
α7

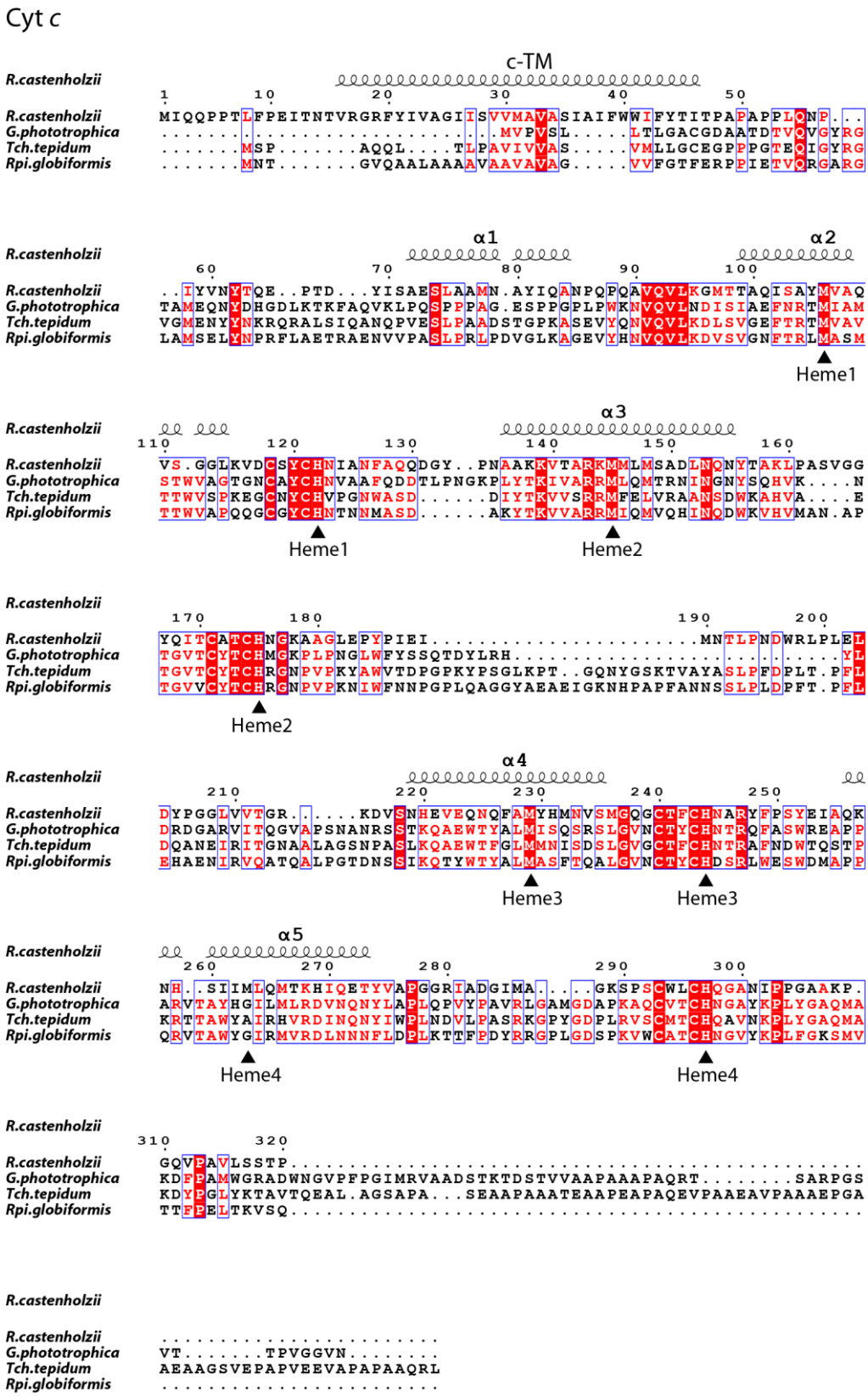

Figure 3—figure supplement 1. Comparison of *Roseiflexus castenholzii* reaction center (RC) with the reported RCs from *Tch.tepidum* (PDB ID: 5Y5S), *G. phototrophica* (PDB ID:

7O0U), *Rpi. globiformis* (PDB ID: 7XXF). (A) Comparison of *R. castenholzii* native RC structure (colored) with that of *G. phototrophica* RC-dLH (gary), *Tch. tepidum* RC-LH1 (purple) and *Rpi. globiformis* RC-LH1 (cornflower blue). The N- and C-terminus of the L and M subunits are labeled and indicated. **(B)** Comparison of *R. castenholzii* cyt *c* structure (yellow-orange, heme-*c* colored in red) with the tetraheme-bound cyt *c* subunit from of *G. phototrophica* RC-dLH (gary), *Tch. tepidum* RC-LH1 (purple) and *Rpi. globiformis* RC-LH1 (cornflower blue). The N-terminus of each cyt *c* subunit is labeled. **(C)** Structure based sequence alignment of the L, M and cyt *c* subunits from *R. castenholzii* and the representative purple bacteria. *Tch.tepidum* (PDB ID: 5Y5S), *G. phototrophica* (PDB ID: 7O0U), *Rpi. globiformis* (PDB ID: 7XXF) and *Rba. sphaeroides* (PDB ID: 7F0L). The amino acid residues essential for coordinating the BChl-Mg and heme-*c* are indicated with black triangles.

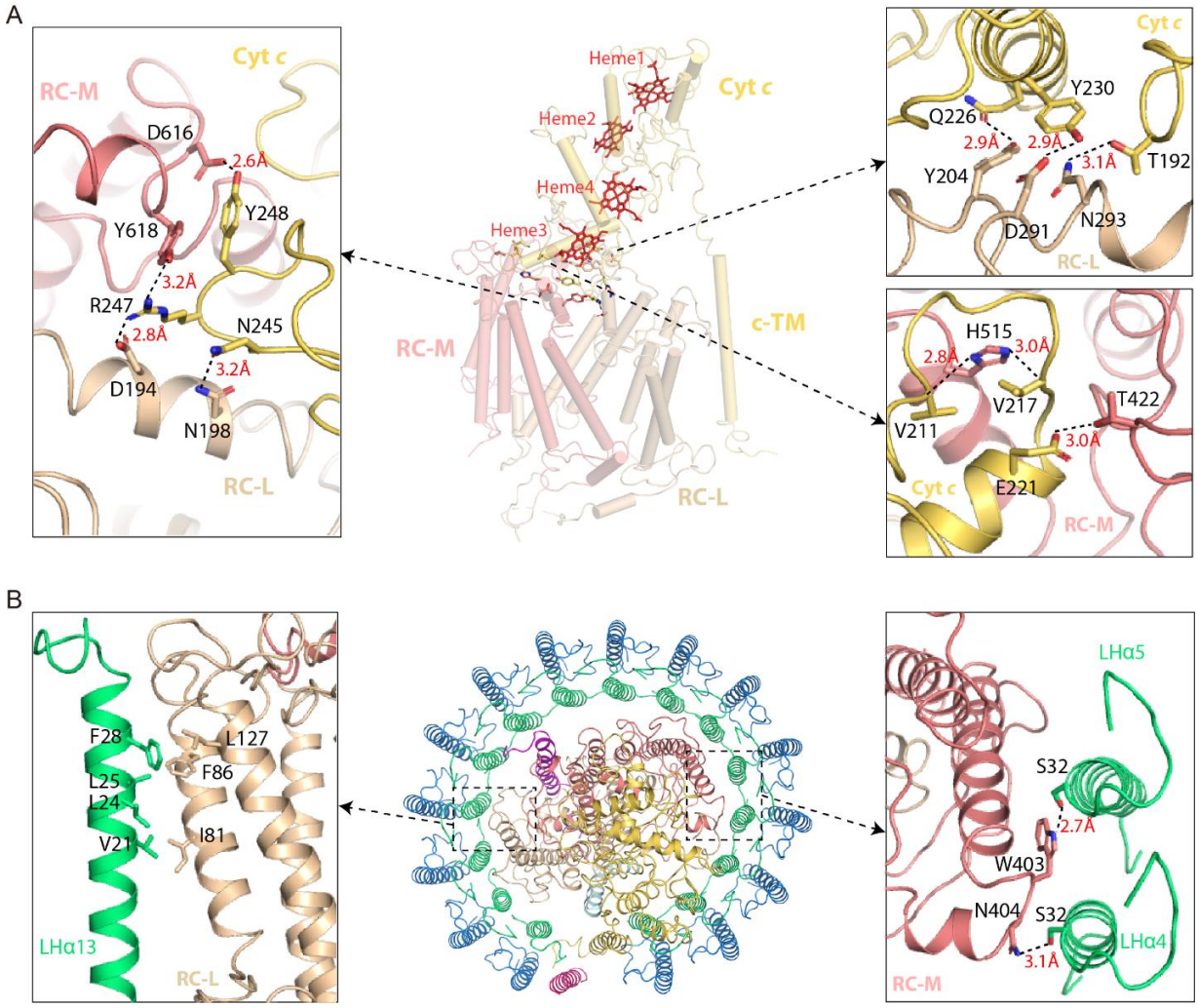

Figure 3—figure supplement 2. Interactions between the LH ring and RC in native RC-LH (nRC-LH) complex from *Roseiflexus castenholzii*. (A) The interactions between cyt *c* (yellow orange) and L (wheat) and M (salmon) subunits of the RC. The side view of RC is shown in middle. L, M and cyt *c* subunits in the RC are shown in cartoon forms, and the *c*-type hemes (red) are shown in stick forms. The zoom-in views of the interactions are shown on the two sides. The amino acid residues involved in the interactions are shown in stick forms. The distances of hydrogen bonding interactions are labeled and indicated with dashed lines. **(B)** The amino acid residues involved in the LH and RC (which is composed of L, M, cyt *c* subunits**)** interactions are shown in stick forms. The general location of the LH and RC contacting area is shown in middle, zoom-in views of the interactions are shown on the two sides.

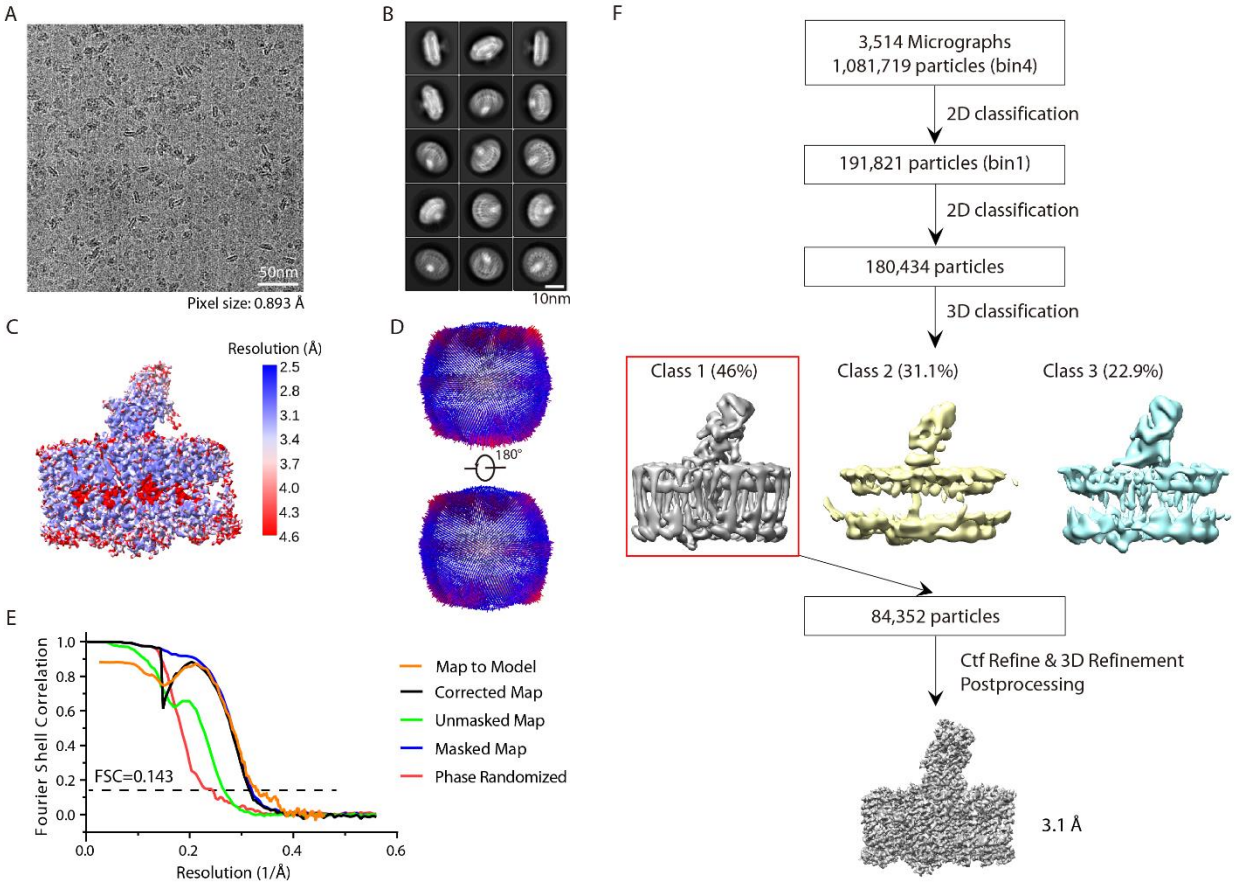

Figure 4—figure supplement 1. Cryo-EM analyses of the carotenoid depleted RC-LH (dRC-LH) complex from *Roseiflexus castenholzii*. (A) A representative raw cryo-EM micrograph of the dRC-LH complex extracted from the fifth sub-culture of DPA-treated *R. castenholzii* cells grown under 10, 000 lux light intensity. **(B)** Representative reference-free 2D class averages of the dRC-LH complex. **(C)** Local resolution of the cryo-EM map estimated by ResMap. **(D)** The different views of angular distribution of the dRC-LH particles in final reconstruction. **(E)** The gold-standard FSC curve of the cryo-EM map (Corrected map, black; Unmasked, green; Masked, blue; Phase randomized, red) and the FSC curve between the map and the final refined model (orange). **(F)** Workflow of the cryo-EM data processing for the carotenoid depleted RC-LH (dRC-LH) complex**.** All structural figures here are generated with ChimeraX.

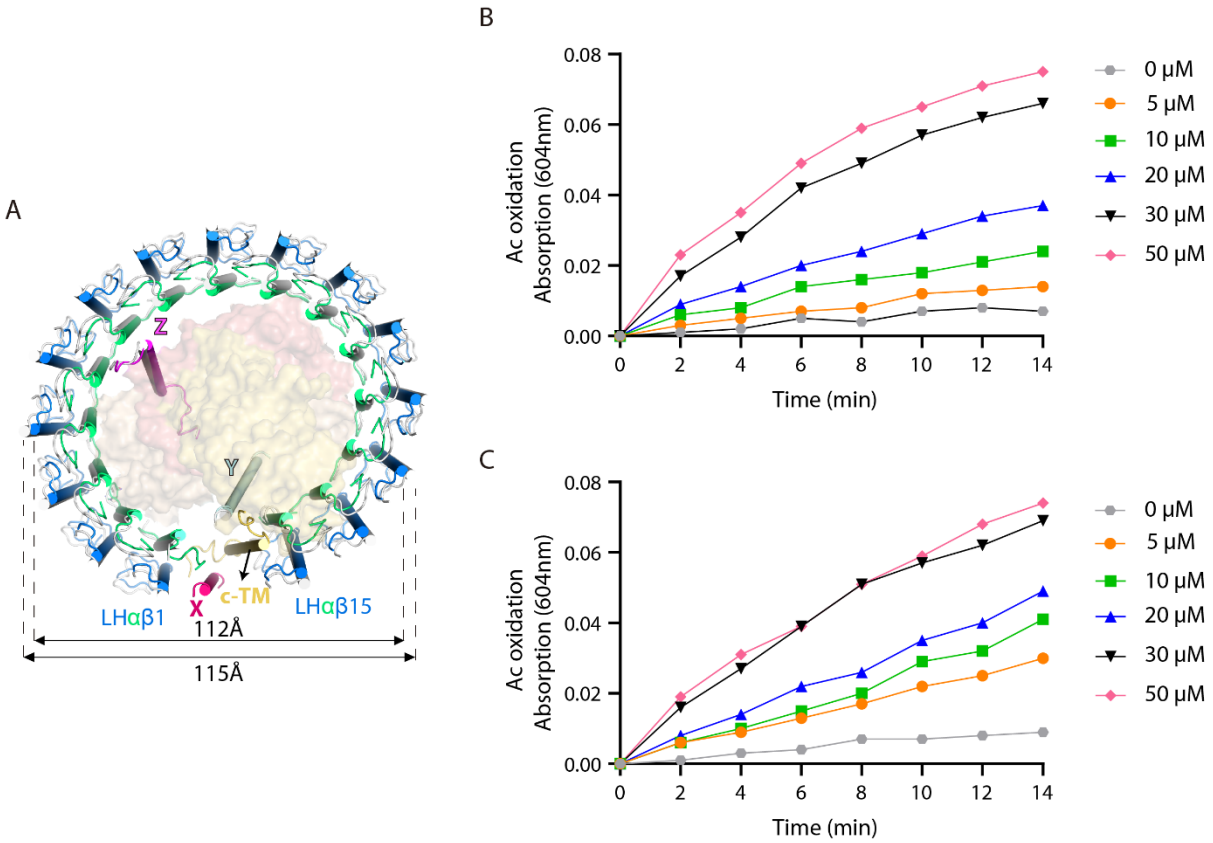

Figure 5—figure supplement 1. The conformational changes and auracyanin (Ac) oxidation activities of the nRC-LH and dRC-LH complexes from *Roseiflexus castenholzii*. **(A)** Superposition of nRC-LH (in color) and dRC-LH (white). Arrows mark the lengths of major axes in the LH ring. The LH ring and RC are shown as cartoon and surface representations, respectively. **(B, C)** Auracyanin (Ac) oxidation assays of the nRC-LH and dRC-LH complexes**.** The absorbance of Ac at 604 nm in presence of the nRC-LH (B) or dRC-LH (C) complex was recorded every 2 min, at 323 K and under 10,000 lx light intensity. Reduced Ac was used as electron donor, and varied concentrations of menaquinone-4 was used as electron acceptor.